Monthly Notices of the ROYAL ASTRONOMICAL SOCIETY

MNRAS **443,** 828–851 (2014) doi:10.1093/mnras/stu1031

The Aquarius comoving group is not a disrupted classical globular cluster★

A. R. Casey,[1,2]† S. C. Keller,[1] A. Alves-Brito,[1,3] A. Frebel,[2] G. Da Costa,[1] A. Karakas,[1] D. Yong,[1] K. C. Schlaufman,[2] H. R. Jacobson,[2] Q. Yu[2] and C. Fishlock[1]

[1]*Research School of Astronomy and Astrophysics, Australian National University, Canberra, ACT 2611, Australia*
[2]*Massachusetts Institute of Technology, Kavli Institute for Astrophysics and Space Research, 77 Massachusetts Avenue, Cambridge, MA 02139, USA*
[3]*Departamento de Astronomía y Astrofísica, Ponticia Universidad Católica de Chile, Av. Vicuña Mackenna 4860, Macul, 782-0436 Santiago, Chile*

Accepted 2014 May 23. Received 2014 May 9; in original form 2013 September 11

ABSTRACT

We present a detailed analysis of high-resolution, high signal-to-noise ratio spectra for five Aquarius stream stars observed with the Magellan Inamori Kyocera Echelle spectrograph on the Magellan Clay telescope. Our sample represents one-third of the 15 known members in the stream. We find the stream is not monometallic: the metallicity ranges from [Fe/H] = −0.63 to −1.58. No anticorrelation in Na–O abundances is present, and we find a strong positive Mg–Al relationship, similar to that observed in the thick disc. We find no evidence that the stream is a result of a disrupted classical globular cluster, contrary to a previously published claim. High [(Na, Ni, α)/Fe] and low [Ba/Y] abundance ratios in the stream suggest that it is not a tidal tail from a disrupted dwarf galaxy, either. The stream is chemically indistinguishable from Milky Way field stars with the exception of one candidate, C222531−145437. From its position, velocity, and detailed chemical abundances, C222531−145437 is likely a star that was tidally disrupted from ω-Centauri. We propose that the Aquarius stream is Galactic in origin, and could be the result of a disc–satellite perturbation in the Milky Way thick disc of the order of a few Gyr ago: derived orbits, *UVW* velocities, and angular momenta of the Aquarius members offer qualitative support for our hypothesis. Assuming that C222531−145437 is a tidally disrupted member of ω-Centauri, this system is the most likely disc perturber. In the absence of compelling chemical and/or dynamical evidence that the Aquarius stream is the tidal tail of a disrupted satellite, we advocate the 'Aquarius group' as a more appropriate description. Like the Canis Major overdensity, as well as the Hercules and Monoceros groups, the Aquarius group joins the list of kinematically identified substructures that are not actually accreted material: they are simply part of the rich complexity of the Milky Way structure.

Key words: Galaxy: halo – Galaxy: structure.

1 INTRODUCTION

Galaxies are formed hierarchically through chaotic mergers of smaller systems, and the Milky Way is no exception (Searle & Zinn 1978; Bullock & Johnston 2005; Helmi 2008). The accumulating stellar debris in our own Galactic halo provides ongoing evidence for such merging events (e.g. Bell et al. 2008). As satellites fall towards the Galaxy, tidal forces disrupt the system, hurtling stars in leading and trailing directions. The position and velocities of stars within these 'stellar streams' are sensitive to the Galactic potential. As such, their phase-space information can collectively constrain the fraction and distribution of accreted matter in the galaxy, the subhalo mass function, as well as the shape and extent of the Milky Way's dark matter halo. Additionally, individual chemical abundances can trace the chemical evolution of the Galaxy and its satellite systems.

Wide-field deep imaging surveys have proved excellent sources for finding stellar streams (e.g. Belokurov et al. 2007). Dozens of streams have been identified through careful photometric selections and matched-filtering techniques, with some to a Galactocentric distance of 100 kpc (e.g. see Drake et al. 2013). This suggests that a large fraction of the stellar halo has been built up by accretion. However, as Helmi & White (1999) point out, these

★This paper includes data gathered with the 6.5 m Magellan Telescopes located at Las Campanas Observatory, Chile.

† E-mail: acasey@mso.anu.edu.au

detection strategies are most successful for identifying streams that are sufficiently distant from the solar neighbourhood. A nearby stream, within ∼10 kpc, will not appear as a photometric overdensity because the stars would be sparsely positioned across the sky. Such substructures would only be detectable by their kinematics, or perhaps with precise elemental abundances through a 'chemical tagging' approach (e.g. see Freeman & Bland-Hawthorn 2002). The confirmation of such substructures would serve to substantially increase the fraction of the known accreted material in the Galaxy.

It is therefore necessary to spectroscopically survey stars in the solar neighbourhood to reveal any nearby substructures. The Radial Velocity Experiment (RAVE) team began such a survey in 2003 and has taken spectra of over 500 000 stars across 17 000 deg^2 (Steinmetz et al. 2006). The primary goal of RAVE is to obtain radial velocities for stars in the solar neighbourhood and beyond. In an attempt to remain kinematically unbiased, RAVE candidates were selected solely by their apparent magnitude ($9 < I < 13$). Almost all have radial velocities published in the RAVE data releases (Steinmetz et al. 2006), and for a subset of stars with a sufficient signal-to-noise ratio (S/N), stellar parameters have been derived by a χ^2-minimization technique (Zwitter et al. 2008; Siebert et al. 2011).

Using these data, Williams et al. (2011) identified a comoving group of nearby ($0.5 \lesssim D \lesssim 10$ kpc) stars near $(l, b) = (60°, -55°)$, in the vicinity of the Aquarius constellation. Thus, the comoving group was named the Aquarius stream. The stream is most apparent when examining heliocentric velocities against Galactic latitude for stars within $-70° < b < -50°$. Williams et al. (2011) employed a selection criteria of $-250 < V_{\rm hel} < -150\,{\rm km\,s^{-1}}$, $30° < l < 75°$ and $J > 10.3$ to maximize the contrast between the stream and stellar background, identifying 15 stars in the process. The average heliocentric velocity of these members was found to be $V_{\rm hel} = -199\,{\rm km\,s^{-1}}$, with a dispersion of $27\,{\rm km\,s^{-1}}$. The radial velocity uncertainties provided by the RAVE catalogue are described to be $\sim 2\,{\rm km\,s^{-1}}$, so that the stream's wide velocity distribution appears to be real.

Through a statistical comparison with predictions of stellar positions and kinematics from the Galaxia (Sharma et al. 2011) and Besançon (Robin et al. 2003) models of the Milky Way, Williams et al. (2011) found the stream to be statistically significant ($>4\sigma$). The choice of model, cell dimension, or extinction rate made no substantial difference to the detection significance. The authors concluded that the overdensity was genuine, and inferred that the comoving group is a stellar stream. Based on the phase-space information available, Williams et al. (2011) concluded that the newly discovered stream could not be positively associated with the Sagittarius or Monoceros stream, the Hercules–Aquila cloud, or either the Canis Major or Virgo overdensities.

RAVE data suggest that the Aquarius stream has a metallicity of [Fe/H] $= -1.0 \pm 0.4$ dex,[1] whereas field stars at the same distance show [Fe/H] $= -1.1 \pm 0.6$ dex after the same selection cuts had been employed. Of the 15 Aquarius stream stars in the Williams et al. (2011) discovery sample, the metallicity range determined from medium-resolution spectroscopy is wide: from [Fe/H] $= -2.02$ to -0.33. High-resolution spectra with high S/N are necessary to accurately characterize the stream's metallicity distribution function.

To this end, Wylie-de Boer et al. (2012) obtained high-resolution ($\mathcal{R} = 25\,000$) spectra with a modest S/N of ∼30 for six Aquarius stream stars using the echelle spectrograph on the Australian National University's 2.3 m telescope. Their data indicate a surprisingly narrow spread in metallicity compared to previous work: [Fe/H] $= -1.09 \pm 0.10$ dex, with a range extending only from -1.25 to -0.98 dex. Samples with such small dispersions in metallicity are typically observed in monometallic environments (e.g. globular or open clusters).

In addition to ascertaining stellar parameters, Wylie-de Boer et al. (2012) measured elemental abundances for the Aquarius stream stars – the only study to date to do so. The authors primarily focused on Na, O, Mg, Al, and Ni. These elements have been extensively studied in globular cluster stars, where unique abundance patterns are observed. Specifically, an anticorrelation between sodium and oxygen content appears ubiquitous to stars in globular clusters (Carretta et al. 2009). Wylie-de Boer et al. (2012) identified two stream stars with slightly higher [Na/Fe] abundance ratios than halo stars of the same metallicity. No strong oxygen depletion was evident in the data, and no overall Na–O anticorrelation was present. Wylie-de Boer et al. (2012) also found [Ni/Fe] abundance ratios similar to thick disc/globular cluster stars, markedly higher than those reported for the Fornax dwarf spheroidal (dSph) galaxy, which has a comparable mean metallicity to the Aquarius stream.

Combined with the low level of [Fe/H] scatter present in their sample, these chemical abundances led Wylie-de Boer et al. (2012) to conclude that the Aquarius stream is the result of a tidally disrupted globular cluster. We note, though, that Williams et al. (2011) previously excluded this scenario after modelling an Aquarius-like progenitor falling towards the Milky Way. The predicted positions and velocities from their simulations could not be reconciled with any known globular cluster, except for ω-Centauri (ω-Cen), although no explicit link was argued. Alternatively, any parent cluster may have been totally disrupted, leaving no identifiable remnant for discovery.

We seek to investigate the nature of the Aquarius stream, specifically the globular cluster origin claimed by Wylie-de Boer et al. (2012). Details of the observations and data reduction are outlined in the following section. The bulk of our analysis is presented in Section 3 and our chemical abundance analysis is chronicled separately in Section 4. A detailed discussion of our results is made in Section 5, and we conclude in Section 6 with a summary of our findings and critical interpretations.

2 OBSERVATIONS AND DATA ANALYSIS

The most complete sample of Aquarius stream stars is presented in the discovery paper of Williams et al. (2011). We have obtained high-resolution, high S/N spectra for five Aquarius stream candidates using the Magellan Inamori Kyocera Echelle (MIKE) spectrograph (Bernstein et al. 2003) on the Magellan Clay telescope. Although these observations were carried out independently of the Wylie-de Boer et al. (2012) study, by chance there are four stars common to both samples. The additional star in this sample, C2306265−085103, was observed by the RAVE survey but had a S/N too low for stellar parameters to be accurately determined. All programme stars were observed in 2011 July in ∼1 arcsec seeing at low airmass (Table 1), and six standard stars were observed in 2011 March. All observations were taken using a 1.0 arcsec slit without spectral or spatial binning, providing a spectral resolution in excess of $\mathcal{R} = 28\,000$ in the blue arm and $\mathcal{R} = 25\,000$ in the red arm. The exposure time for our programme stars was 650 s per star in order to ensure a S/N in excess of 100 pixel^{-1} at 600 nm.

[1] Williams et al. (2011) formally quote [M/H], but for the sake of a consistent discussion we assume [M/H] ≡ [Fe/H] throughout this study.

Table 1. Observations and radial velocities.

Designation	α (J2000)	δ (J2000)	V (mag)	$B-V$	UT Date	UT Time	t_{exp} (s)	S/N[a] (px^{-1})	V_{hel} (km s^{-1})
Standard stars									
HD 41667	06:05:03.7	−32:59:36.8	8.52	0.76	2011-03-13	23:40	90	340	297.1
HD 44007	06:18:48.6	−14:50:44.2	8.06	0.79	2011-03-13	23:52	120	280	161.8
HD 76932	08:58:44.2	−16:07:54.2	5.86	0.53	2011-03-14	00:16	25	330	117.8
HD 136316	15:22:17.2	−53:14:13.9	8.77	1.12	2011-03-14	09:37	120	400	−38.8
HD 141531	15:49:16.9	+09:36:42.5	9.28	1.03	2011-03-14	09:52	120	350	2.8
HD 142948	16:00:01.6	−53:51:04.1	9.27	0.60	2011-03-14	09:45	90	320	29.9
Programme stars									
C222531−145437	22:25:31.7	−14:54:39.6	12.49	1.20	2011-07-30	06:52	650	135	−156.4
C230626−085103	23:06:26.6	−08:51:04.8	12.60	1.28	2011-07-30	08:15	650	100	−221.1
J221821−183424	22:18:21.2	−18:34:28.3	12.12	0.96	2011-07-30	05:58	650	115	−159.5
J223504−152834	22:35:04.5	−15:28:34.9	12.26	1.02	2011-07-30	07:34	650	130	−169.7
J223811−104126	22:38:11.6	−10:41:29.4	11.93	0.79	2011-07-30	08:57	650	115	−235.7

[a]S/N measured per pixel (∼0.09 Å px^{-1}) at 600 nm for each target.

Calibration frames were taken at the start of each night, including 20 flat-field frames (10 quartz lamp, 10 diffuse flats) and 10 Th–Ar arc lamp exposures. The data were reduced using the CARPY pipeline.[2] For comparison purposes one of the standard stars, HD 41667, was also reduced using standard extraction and calibration methods in IRAF. The resultant spectra from both approaches were compared for residual fringing, S/N, and wavelength calibration. No noteworthy differences were present, and the CarPy pipeline was utilized for the remainder of the data reduction. Each reduced echelle order was carefully normalized using a cubic spline with defined knot spacing. Normalized orders were stitched together to provide a single one-dimensional spectrum from 333 to 916 nm. A portion of normalized spectra for the programme stars is shown in Fig. 1.

The white dwarf HR 6141 was observed in 2011 March as a telluric standard. The S/N for HR 6141 exceeds that of any of our standard or programme stars. Although the atmospheric conditions at Las Campanas Observatory are certain to change throughout the night and between observing runs, we are primarily using this spectrum to identify stellar absorption lines that are potentially affected by telluric absorption.

3 ANALYSIS

3.1 Radial velocities

The radial velocity for each star was determined in a two-step process. An initial estimate of the radial velocity was ascertained by cross-correlation with a synthetic spectrum of a giant star with $T_{\rm eff} = 4500$ K, $\log g = 1.5$, and [Fe/H] = −1.0 across the wavelength range 845 to 870 nm. The observed spectrum was shifted to the pseudo-rest frame using this initial velocity estimate. Equivalent widths (EWs) were measured for ∼160 atomic transitions by integrating fitted Gaussian profiles (see Section 3.2). In each case a residual line velocity was calculated from the expected rest wavelength and the measured wavelength. The mean residual velocity offset correction is small in all cases (<1 km s^{-1}), and this residual correction is applied to the initial velocity measurement from cross-correlation. The final heliocentric velocities are listed in Table 1, where the typical uncertainty is ±0.1 km s^{-1}. These velocities agree quite well with those compiled by Williams et al. (2011) as part of the RAVE survey: the mean offset of 2.5 km s^{-1} with a standard deviation of 2.7 km s^{-1}.

3.2 Line measurements

For the measurement of atomic absorption lines, we employed the line list of Yong, Carney & Teixera de Almeida (2005) with additional transitions of Cr, Sc, Zn, and Sr from Roederer et al. (2010). The list has been augmented with molecular CH data from Plez, Masseron & Van Eck (2008). For molecular features (e.g. CH), or lines with hyperfine and/or isotopic splitting (Sc, V, Mn, Co, Cu, Ba, La and Eu), we determined the abundance using spectral synthesis with the relevant data included. Isotopic and hyperfine splitting data was taken from Kurucz & Bell (1995) for Sc, V, Mn, Co and Cu, Biémont, Palmeri & Quinet (1999) for Ba, Lawler, Bonvallet & Sneden (2001a) for La, and Lawler et al. (2001b) for Eu. For all other transitions, abundances were obtained using the measured EWs.

The EWs for all absorption lines were measured automatically using software written during this study. The local continuum surrounding every atomic transition is determined, and a Gaussian profile is iteratively fit to the absorption feature of interest. Our algorithm accounts for crowded or blended regions by weighting pixels as a function of difference to the rest wavelength. These algorithms and software are fully outlined in Casey (2014). For this study, we have verified our approach by comparing EWs of 156 lines measured by hand and tabulated in Norris, Ryan & Beers (1996). We only included measurements in the Norris et al. (1996) study that were not marked by Norris et al. (1996) to have questionable line quality parameters. Excellent agreement is found between the two studies, which is illustrated in Fig. 2. The mean difference is a negligible −0.64 ± 2.78 mÅ, and no systematic trend is present. The scatter can be attributed to the lack of significant digits in the Norris et al. (1996) study, as well as the S/N of the data. Other studies (e.g. Frebel, Casey, Jacobson & Yu 2013) using the same algorithm used here find better agreement for spectra with higher S/N: 0.20 ± 0.16 mÅ when we compare our results with manual measurements by Aoki et al. (2007), and a difference of 0.25 ± 0.28 mÅ is found

[2] http://code.obs.carnegiescience.edu/mike

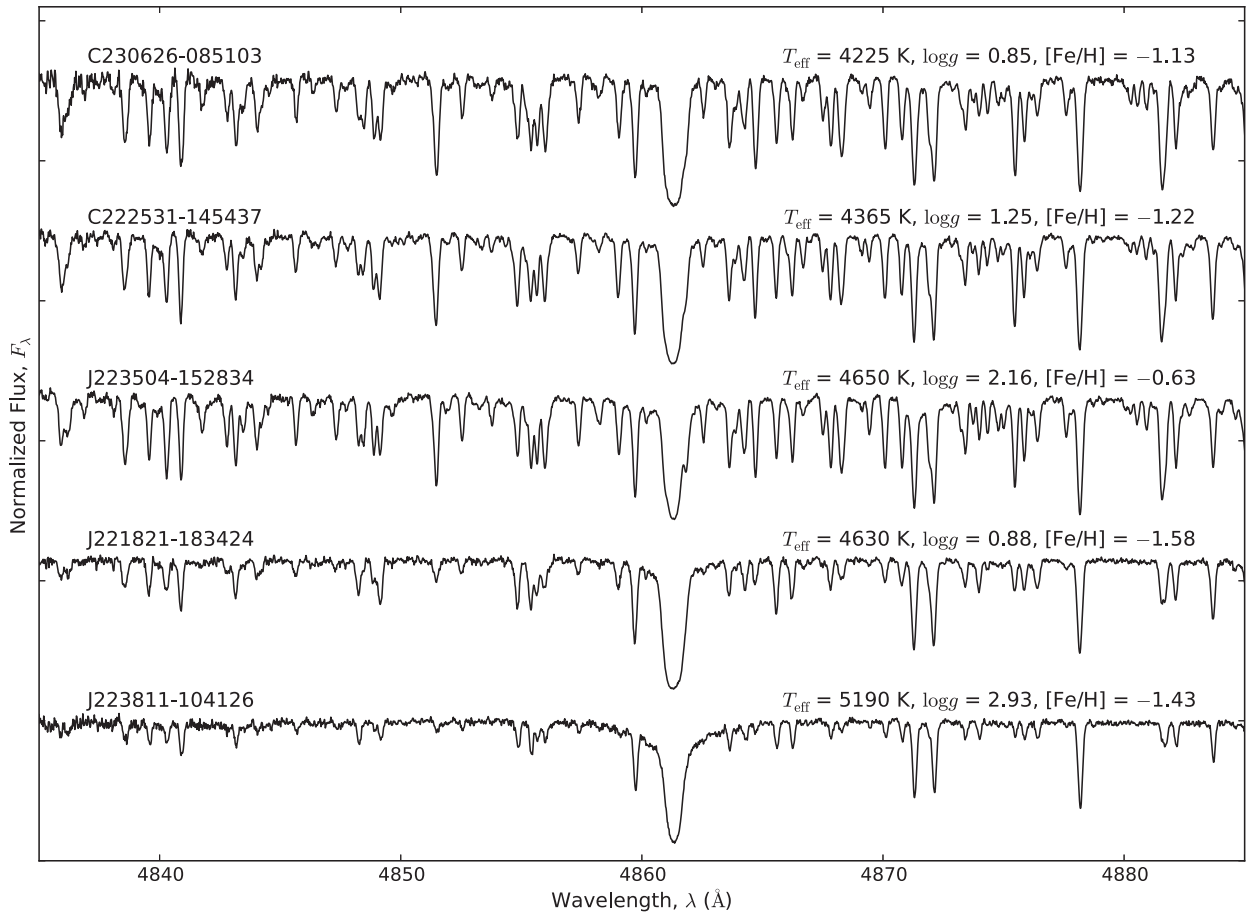

Figure 1. Normalized rest-frame spectra surrounding the H–β absorption line for all Aquarius stream candidates with offset fluxes. The effective temperature, surface gravity and metallicity is shown for all stars.

between manual measurements by Cayrel et al. (2004) and our automatic results. Although we are extremely confident in our EW measurements, *every* absorption profile was repeatedly examined by eye for quality, and spurious measurements were removed.

We list the atomic data and measured EWs in Table 2. Transitions near the flat portion of the curve-of-growth have been excluded by removing measurements with reduced equivalent widths (REW), $\log_{10}({\rm EW}/\lambda) > -4.5$. A minimum detectable EW was calculated as a function of wavelength, S/N and spectral resolution following Norris, Ryan & Beers (2001),

$$\mathrm{EW_{min}} \approx \left(\frac{S}{N}\right)^{-1} \sqrt{1.5 \times \mathrm{FWHM} \times \delta\lambda}, \quad (1)$$

where FWHM is the minimum detectable line profile limited by instrumental broadening and $\delta\lambda$ is the pixel size. Only lines that exceeded a 3σ detection significance were included for this analysis.

3.3 Model atmospheres

We have employed the ATLAS9 plane-parallel stellar atmospheres of Castelli & Kurucz (2003). These one-dimensional models ignore any centre-to-limb spatial variations, assume hydrostatic equilibrium and no convective overshoot from the photosphere. The stellar parameter spacing between models is 250 K in temperature, 0.5 dex in surface gravity, 0.5 dex in [M/H] and 0.4 dex in [α/Fe]. We interpolated the temperature, gas and radiative pressure, electron density and opacities between atmosphere models using the Quickhull algorithm (Barber, Dobkin & Huhdanpaa 1996). Quickhull is reliant on Delaunay tessellation, which suffers from extremely skewed cells when the grid points vary in size by orders of magnitude – as $T_{\rm eff}$ values do compared to log g or [(M,α)/H]. If unaccounted for, performing interpolation using such asymmetric cells can result in significant errors in atmospheric properties across all photospheric depths. We scaled each stellar parameter between zero and unity before interpolation to minimize these interpolation errors.

3.4 Stellar parameters

The 2011 May version of the MOOG (Sneden 1973) spectral synthesis code has been used to derive individual line abundances and stellar parameters. This version employs Rayleigh scattering (Sobeck et al. 2011) instead of treating scattering as true absorption, which is particularly important for transitions blueward of 450 nm. This is noteworthy, but is less relevant for these analyses as most of the atomic transitions utilized here are redward of 450 nm.

3.4.1 Effective temperature

The effective temperature, $T_{\rm eff}$, for each star was found by demanding a zero-trend in excitation potential and line abundance for measurable Fe I transitions. The data were fitted with a linear slope, and gradients less than $|10^{-3}|$ dex eV^{-1} were considered to be

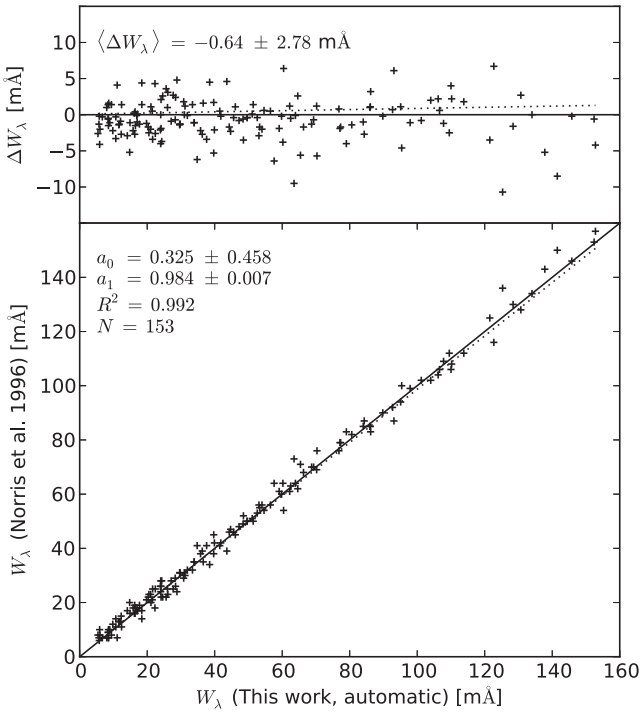

Figure 2. Comparison showing EWs measured for HD 140283 using our automatic routine (see Section 3.2), and manual measurements by Norris et al. (1996). No systematic trend is present, and the mean difference between these studies is $\langle \Delta W_\lambda \rangle = -0.64 \pm 2.78$ mÅ. The offset (a_0) and the slope (a_1) of the fit are shown.

converged. For comparison, photometric temperatures were calculated after our spectroscopic temperatures had been derived, and these are discussed in Section 3.4.4.

3.4.2 *Microturbulence and surface gravity*

The microturbulence for each star was found by forcing a zero-trend in the REW and abundance for Fe I lines. Similar to the effective temperature, linear slopes in REW and abundance of less than $|10^{-3}|$ dex were considered converged. The surface gravity for all stars was found by forcing the mean Fe I and Fe II abundances to be equal. A tolerance of $|\langle \mathrm{Fe\,I} \rangle - \langle \mathrm{Fe\,II} \rangle| \leq 0.05$ was deemed acceptable. The process is iterative: a zero-trend with the excitation potential, REW and abundances must be maintained. A solution was only adopted when the all criteria were simultaneously satisfied.

3.4.3 *Metallicity*

The model atmosphere metallicity was exactly matched to that of our mean Fe I abundance. Individual Fe line abundances that were unusually deviant (e.g. $>3\sigma$) from the mean abundance were removed. The largest number of outlier measurements removed for any observation was nine for C222531−145437. These were transitions near the flat part of the curve-of-growth with REWs ~ -4.5, leaving 60 Fe I and 10 Fe II lines for the analysis of C222531−145437. Usually only one outlier measurement was removed for the other candidates. The minimum number of Fe transitions employed for stellar parameter determination was 42 lines (33 Fe I and 9 Fe II), which occurred for our hottest star, J223811−104126.

3.4.4 *Photometric effective temperatures*

As a consistency check for our spectroscopic temperatures, we have estimated effective temperatures using the colour–$T_{\rm eff}$ empirical relationship for giant stars from Ramírez & Meléndez (2005). The $V - K$ colour has been employed as its calibration has the lowest residual fit. This relationship has a slight dependence on metallicity, and as such we have adopted the spectroscopic [Fe/H] values in Table 3 for these calculations. Optical V-band magnitudes from the APASS catalogue (Henden et al. 2012) have been employed, and K-band magnitudes have been sourced from the 2MASS catalogue (Skrutskie et al. 2006). The reddening maps of Schlegel, Finkbeiner & Davis (1998) estimate that the extinction for our stars varies between $E(B - V) = 0.03$ to 0.07 mag, and these values have been used to de-redden our $V - K$ colour.

Calculated photometric temperatures are listed in Table 4. The mean difference between the photometric temperatures and those found by excitation balance is −19 K, where the largest variation is −93 K for J223504−152834. While these photometric temperatures serve as a confirmation for our spectroscopically derived values, for the remainder of this analysis we have employed effective temperatures determined by excitation balance.

3.5 Uncertainties in stellar parameters

Due to scatter in neutral iron lines measurements, there is a formal uncertainty in our calculated trend line between excitation

Table 2. List of atomic transitions and equivalent width measurements for programme and standard stars.

Wavelength (Å)	Species	χ (eV)	log gf	Equivalent width C222531−145437 (mÅ)	C2306265−085103 (mÅ)	J221821−183424 (mÅ)	J223504−152834 (mÅ)	J223811−104126 (mÅ)	(Cont.)
6300.30	O I	0.00	−9.72	45.4	66.9	38.5	32.8	17.9	
6363.78	O I	0.02	−10.19	19.5	28.3	13.0	18.8	–	
5688.19	Na I	2.11	−0.42	–	–	49.0	131.5	38.4	
6154.23	Na I	2.10	−1.53	24.1	38.9	–	48.5	–	
6160.75	Na I	2.10	−1.23	37.7	58.5	–	65.7	–	
6318.72	Mg I	5.11	−1.97	–	47.9	14.7	62.8	8.9	
6319.24	Mg I	5.11	−2.22	30.8	–	5.5	–	–	
6965.41	Mg I	5.75	−1.51	–	–	–	59.2	–	

Table 2 is published in its entirety in the electronic edition. A portion is shown here for guidance regarding its form and content.

Table 3. Stellar parameters for standard and programme stars.

Designation	*This study* $T_{\rm eff}$ (K)	$\log g$ (dex)	ξ_t (km s^{-1})	[Fe/H] (dex)	*Literature* $T_{\rm eff}$ (K)	$\log g$ (dex)	ξ_t (km s^{-1})	[Fe/H] (dex)	Reference
					Standard stars				
HD 41667	4660	1.71	1.84	−1.20	4605	1.88	1.44	−1.16	Gratton et al. (2000)
HD 44007	4835	1.78	1.95	−1.77	4850	2.00	2.20	−1.71	Fulbright (2000)
HD 76932	5800	3.88	1.65	−1.05	5849	4.11	–	−0.88	Nissen et al. (2000)
HD 136316	4355	0.58	2.06	−1.93	4414	0.94	1.70	−1.90	Gratton & Sneden (1991)
HD 141531	4345	0.63	2.07	−1.69	4280	0.70	1.60	−1.68	Shetrone (1996)
HD 142948	5025	2.25	2.05	−0.74	4713	2.17	1.38	−0.77	Gratton et al. (2000)
					Programme stars				
C222531−145437	4365	1.25	1.94	−1.22	4235 ± 118	1.45 ± 0.21	1.96 ± 0.11	−1.20 ± 0.14	Wylie-de Boer et al. (2012)
C230626−085103	4225	0.85	1.92	−1.13	–	–	–	–	–
J221821−183424	4630	0.88	2.16	−1.58	4395 ± 205	1.45 ± 0.35	1.96 ± 0.18	−1.15 ± 0.21	Wylie-de Boer et al. (2012)
J223504−152834	4650	2.16	1.55	−0.63	4597 ± 158	2.40 ± 0.14	1.47 ± 0.07	−0.98 ± 0.17	Wylie-de Boer et al. (2012)
J223811−104126	5190	2.93	1.62	−1.43	5646 ± 147	4.60 ± 0.15	1.09 ± 0.11	−1.20 ± 0.20	Wylie-de Boer et al. (2012)

Table 4. Reddening and photometric temperatures for programme stars.

Designation	$E(B-V)$ (mag)	$(V-K)_0$ (mag)	$T_{\rm phot}$ (K)	$T_{\rm spec}$ (K)	ΔT (K)
C222531−145437	0.03	2.86	4285	4365	−80
C230626−085103	0.05	3.00	4196	4225	−29
J221821−183424	0.03	2.36	4685	4630	+55
J223504−152834	0.04	2.50	4557	4650	−93
J223811−104126	0.07	1.84	5240	5190	+50

potential and abundance, as well as between the REW and abundance. We have calculated 1σ uncertainties in effective temperature and microturbulence by independently varying each stellar parameter until the relevant slope matches that formal uncertainty. This process is repeated for positive and negative offsets in temperature and microturbulence to allow for asymmetric uncertainties. The largest absolute offset is taken as the 1σ uncertainty. For surface gravity, the uncertainty has been calculated by varying $\log g$ until the difference in mean Fe I–Fe II abundance matches the standard error about the mean for Fe I and Fe II in quadrature. The calculated uncertainties are tabulated in Table 5.

Table 5. Uncorrelated uncertainties in stellar parameters for standard and programme stars.

Designation	$\sigma(T_{\rm eff})$ (K)	$\sigma(\xi_t)$ (km s^{-1})	$\sigma(\log g)$ (dex)
HD 41667	53	0.09	0.13
HD 44007	81	0.29	0.09
HD 76932	107	0.08	0.19
HD 136316	33	0.15	0.12
HD 141531	25	0.05	0.13
HD 142948	47	0.10	0.11
J221821−183424	42	0.11	0.09
C222531−145437	46	0.05	0.12
J223504−152834	61	0.08	0.05
J223811−104126	49	0.16	0.08
C230626−085103	52	0.05	0.04

These uncertainties ignore any correlations between stellar parameters, and therefore are likely to be underestimated. As such, we have assumed the total uncertainty in stellar parameters to be $\sigma(T_{\rm eff}) = \pm 125$ K, $\sigma(\log g) = \pm 0.30$ dex, and $\sigma(\xi_t) = \pm 0.20$ km s^{-1}. These adopted uncertainties are higher than those listed in Table 5, and can be regarded as extremely conservative.

3.6 Distances

Distances to the Aquarius stars are necessary for understanding the dynamical history of the parent cluster. Many groups have determined distances for stars in the RAVE survey catalogue, which includes all Aquarius stream members. Williams et al. (2011) tabulated a range of distances inferred by different techniques. Not every measurement technique was applicable to all Aquarius stars. The reduced proper motion distance technique was the only method to estimate distances for all Aquarius candidates. The variations between distance measurements are large. In particular, the distance for C222531−146537 ranged from 1.4 ± 0.1 kpc (Burnett & Binney 2010) to 10.3 ± 2.4 kpc (Breddels et al. 2010), where both groups claim to have the 'most likely' distances.

Using the stellar parameters tabulated in Table 3, we have calculated distances by isochrone fitting. The Dotter et al. (2008) α-enhanced isochrones were used for these calculations, and an age of 10 Gyr was assumed for all stars (Williams et al. 2011; Wylie-de Boer et al. 2012). The closest point to the isochrone was found by taking the uncertainties in $T_{\rm eff}$ and $\log g$ (see Section 3.5) into account and measuring the distance modulus in the J band. Given the (i) number of uncertain measurements involved in calculating distances ($T_{\rm eff}$, $\log g$, $E(B-V)$, J) and (ii) the resultant asymmetric uncertainties, distances were determined from 10 000 Monte Carlo realizations. Table 6 lists the input parameters and uncertainties adopted for the Monte Carlo realizations, as well as the emergent distances and uncertainties. Uncertainties in input parameters were assumed to be normally distributed. Of the distance scales collated in Williams et al. (2011), our distances are in most agreement with the Zwitter et al. (2010) system. In fact, we find the best agreement with the mean of all the distance scales tabulated in Williams et al. (2011). The uncertainties in our distance determinations are of the order of 20 per cent.

Table 6. Parameters and uncertainties for Monte Carlo realizations.

	Input parameters for Monte Carlo simulation							**Output**
Designation	$T_{\rm eff}$ (K)	$\log g$ (dex)	J (mag)	$E(B-V)$ (mag)	$V_{\rm hel}$ (km s^{-1})	μ_α (mas yr^{-1})	μ_δ (mas yr^{-1})	D (kpc)
C222531−145437	4365 ± 125	1.25 ± 0.20	10.341 ± 0.022	0.03 ± 0.01	−156.4 ± 0.1	3.5 ± 2.1	−14.7 ± 2.2	$5.1^{+1.1}_{-0.8}$
C230626−085103	4225 ± 125	0.85 ± 0.20	10.312 ± 0.025	0.05 ± 0.01	−221.1 ± 0.1	−2.5 ± 2.8	−15.4 ± 2.7	$6.5^{+1.4}_{-1.1}$
J221821−183424	4630 ± 125	0.88 ± 0.20	10.340 ± 0.021	0.03 ± 0.01	−159.5 ± 0.1	−10.6 ± 2.5	−19.3 ± 2.5	$5.6^{+1.3}_{-0.9}$
J223504−152834	4650 ± 125	2.16 ± 0.20	10.363 ± 0.025	0.04 ± 0.01	−169.7 ± 0.1	15.9 ± 2.2	−12.8 ± 2.2	$1.9^{+0.5}_{-0.4}$
J223811−104126	5190 ± 125	2.93 ± 0.20	10.420 ± 0.018	0.07 ± 0.01	−235.7 ± 0.1	−25.3 ± 2.1	−99.5 ± 2.1	$1.1^{+0.3}_{-0.2}$

3.7 Dynamics

Velocity vectors and Galactic orbits have been determined in the same Monte Carlo realizations outlined in Section 3.6, which includes uncertainties in distances, proper motions[3] and heliocentric velocities. We assume no uncertainty in on-sky position (α, δ). Orbital energy calculations have assumed a three-component (bulge, disc, halo) model of the Galactic potential that reasonably reproduces the Galactic rotation curve. The bulge is represented by a Hernquist potential:

$$\Phi_{\rm bulge}(x, y, z) = \frac{GM_b}{r + a}, \tag{2}$$

where $a = 0.6$ kpc. The disc is modelled as a Miyamoto–Nagai potential (Miyamoto & Nagai 1975), where

$$\Phi_{\rm disc}(x, y, z) = \frac{GM_{\rm disc}}{\sqrt{x^2 + y^2 + (b + \sqrt{z^2 + c^2})^2}}, \tag{3}$$

with $b = 4.5$ kpc and $c = 0.25$ kpc and the Galactic halo is represented by a Navarro–Frenk–White dark matter halo (Navarro, Frenk & White 1997):

$$\Phi_{\rm halo} = -\frac{GM_{\rm vir}}{r\left[\log(1 + c) - c/(1 + c)\right]} \log\left(1 + \frac{r}{r_{\rm s}}\right), \tag{4}$$

with the three components scaled such that the disc provides 85 per cent of the radial force at $R_{\rm GC}$, in order to yield a flat circular-speed curve at $R_{\rm GC}$. The solar motion of Schönrich (2012) has been adopted, where $R_{\rm GC} = 8.27$ kpc and a circular velocity speed $V_{\rm c} = 238$ km s^{-1}.

The Aquarius stream members have bound orbits, all of which are probably retrograde except for J223504−152834 (Fig. 3). Orbital energies and angular momenta from Monte Carlo simulations are illustrated in Fig. 4. The 16 686 stars from the Geneva–Copenhagen Survey sample (Nordström et al. 2004) are also shown as a reference, which primarily consists of nearby disc stars.

4 CHEMICAL ABUNDANCES

We have scaled our chemical abundances to solar values using the chemical composition described in Asplund et al. (2009). The abundances for the standard and programme stars are shown in Tables 7 and 8, respectively. The discussion of comparable elements are grouped accordingly.

[3] The proper motions in table 1 of Williams et al. (2011) are erroneous in that they are associated with the wrong stars. The error was typographical and did not affect the transverse velocity calculations (Williams, private communication). The proper motions listed in our Table 6 are correct.

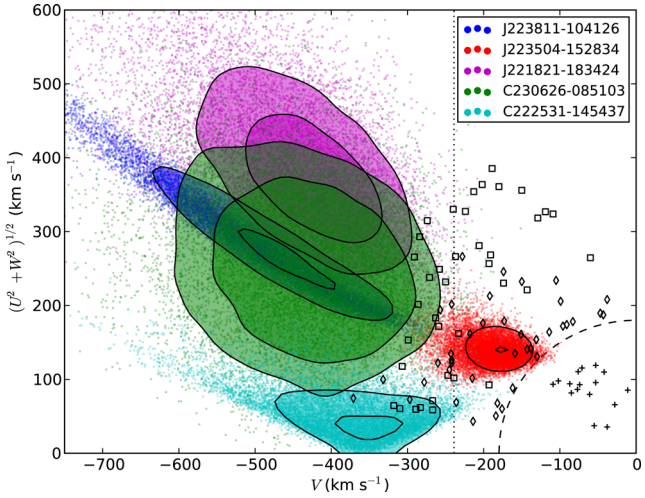

Figure 3. Galactic plane rotational velocities versus out-of-plane total velocities. The contours of each star represent the 68 and 95 per cent confidence intervals from 10 000 Monte Carlo realizations of the parameter distributions shown in Table 6. A sample of thick disc data from Nissen & Schuster (2010) is shown (+), as well as their high- and low-α halo populations ($\diamond$ and ◯, respectively).

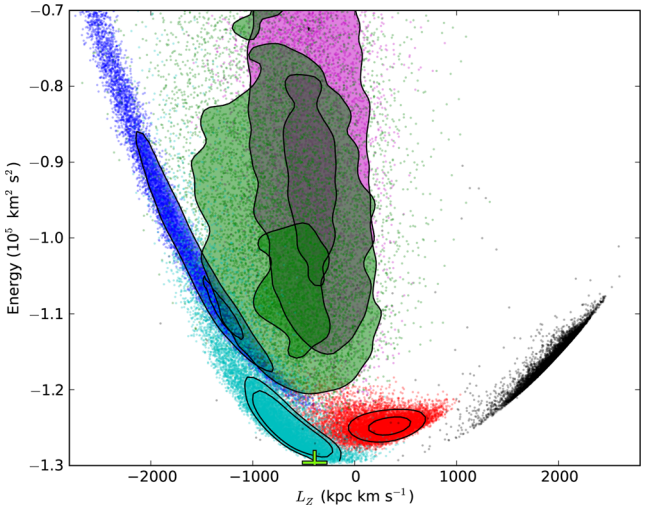

Figure 4. A Linblad ($L_Z - E$) diagram showing angular momenta and orbital energies after 10 000 Monte Carlo realizations for each Aquarius stream star. Isocontours represent the 68 and 95 per cent confidence intervals. ω-Cen is shown as a lime green marker (Wylie-de Boer, Freeman & Williams 2010). The black points without contours are from the Geneva–Copenhagen Survey sample (Nordström et al. 2004), which primarily consists of nearby disc stars and serves as a validation of our orbital energy calculations. Colours are the same as in Fig. 3.

Table 7. Standard star abundances.

Species	N	$\log\epsilon(X)$	σ	[X/H]	[X/Fe]	Species	N	$\log\epsilon(X)$	σ	[X/H]	[X/Fe]
		HD 41667						HD 44007			
C (CH)	2	6.95	0.20	−1.48	−0.28	C (CH)	2	6.66	0.20	−1.77	−0.01
O I	2	7.95	0.06	−0.74	0.46	O I	1	7.41	0.00	−1.28	0.48
Na I	3	4.90	0.18	−1.34	−0.14	Na I	2	4.44	0.09	−1.80	−0.04
Mg I	4	6.72	0.10	−0.88	0.32	Mg I	2	6.30	0.06	−1.29	0.47
Al I	4	5.18	0.11	−1.27	−0.07	Al I	1	:4.80	–	:−1.65	:0.11
Si I	5	6.55	0.06	−0.96	0.24	Si I	5	6.07	0.07	−1.44	0.32
K I	1	4.64	–	−0.39	0.81	K I	1	4.31	–	−0.72	1.04
Ca I	4	5.47	0.06	−0.87	0.33	Ca I	4	4.95	0.02	−1.39	0.37
Sc II	5	2.00	0.12	−1.15	0.05	Sc II	5	1.32	0.12	−1.85	−0.07
Ti I	4	3.96	0.04	−0.99	0.21	Ti I	1	3.48	–	−1.47	0.29
Ti II	3	4.09	0.25	−0.86	0.35	Ti II	4	3.47	0.15	−1.48	0.28
V I	4	2.85	0.11	−1.08	0.12	V I	1	2.22	–	−1.72	0.05
Cr I	10	4.22	0.08	−1.42	−0.22	Cr I	15	3.65	0.07	−1.99	−0.22
Cr II	2	4.54	0.05	−1.09	0.11	Cr II	3	4.00	0.01	−1.64	0.12
Mn I	3	3.87	0.04	−1.56	−0.36	Mn I	2	3.21	0.06	−2.22	−0.48
Fe I	61	6.30	0.12	−1.20	0.00	Fe I	51	5.74	0.13	−1.76	0.00
Fe II	13	6.35	0.05	−1.15	0.05	Fe II	15	5.74	0.10	−1.76	−0.00
Co I	3	3.73	0.06	−1.26	−0.06	Co I	0	–	–	–	–
Ni I	7	4.94	0.12	−1.28	−0.08	Ni I	4	4.47	0.05	−1.75	0.01
Cu I	1	2.29	–	−1.90	−0.70	Cu I	1	1.58	–	−2.61	−0.85
Zn I	2	3.36	0.08	−1.20	0.00	Zn I	2	2.83	0.05	−1.73	0.03
Sr II	1	1.59	–	−1.28	−0.08	Sr II	2	1.13	0.09	−1.75	0.01
Y II	5	0.97	0.19	−1.24	−0.04	Y II	6	0.28	0.11	−1.93	−0.16
Zr I	2	1.42	0.05	−1.17	0.04	Zr I	0	–	–	–	–
Zr II	1	1.28	–	−1.30	−0.10	Zr II	1	0.59	–	−1.99	−0.23
Ba II	2	0.95	0.07	−1.23	−0.02	Ba II	2	0.31	0.06	−1.87	−0.11
La II	1	0.17	–	−0.93	0.27	La II	2	−0.57	0.05	−1.67	0.09
Ce II	4	0.35	0.18	−1.23	−0.02	Ce II	3	−0.41	0.12	−1.99	−0.23
Nd II	9	0.54	0.10	−0.88	0.32	Nd II	9	−0.36	0.11	−1.78	−0.01
Eu II	1	−0.13	–	−0.65	0.55	Eu II	1	−1.16	–	−1.68	0.08
		HD 76932						HD 136316			
C (CH)	2	7.52	0.20	−0.91	0.14	C (CH)	2	5.95	0.20	−2.48	−0.50
O I	1	8.05	–	−0.64	0.41	O I	1	7.17	–	−1.52	0.41
Na I	3	5.37	0.04	−0.87	0.18	Na I	2	4.17	0.04	−2.08	−0.14
Mg I	3	6.95	0.20	−0.65	0.40	Mg I	2	6.08	0.24	−1.52	0.41
Al I	4	5.45	0.07	−1.00	0.05	Al I	0	–	–	–	–
Si I	5	6.79	0.06	−0.72	0.33	Si I	4	5.89	0.05	−1.62	0.31
K I	1	4.94	–	−0.09	0.96	K I	1	3.91	–	−1.12	0.81
Ca I	4	5.60	0.02	−0.74	0.31	Ca I	4	4.71	0.02	−1.63	0.30
Sc II	4	2.10	0.05	−1.05	0.01	Sc II	4	1.20	0.08	−1.95	−0.02
Ti I	1	4.36	–	−0.59	0.46	Ti I	3	3.19	0.03	−1.76	0.17
Ti II	3	4.33	0.04	−0.62	0.44	Ti II	3	3.44	0.10	−1.51	0.42
V I	1	:3.33	–	:−0.60	:0.45	V I	3	1.85	0.01	−2.08	−0.15
Cr I	15	4.46	0.05	−1.18	−0.13	Cr I	12	3.49	0.05	−2.15	−0.22
Cr II	3	4.76	0.02	−0.88	0.17	Cr II	2	3.90	0.02	−1.74	0.19
Mn I	3	4.09	0.06	−1.34	−0.28	Mn I	3	3.09	0.03	−2.34	−0.41
Fe I	51	6.45	0.10	−1.05	0.00	Fe I	62	5.57	0.11	−1.93	0.00
Fe II	13	6.50	0.07	−1.00	0.05	Fe II	14	5.61	0.12	−1.89	0.04
Co I	1	3.94	–	−1.05	0.00	Co I	2	2.95	0.11	−1.09	−0.11
Ni I	5	5.29	0.02	−0.93	0.13	Ni I	5	4.22	0.11	−2.00	−0.07
Cu I	1	2.53	–	−1.66	−0.61	Cu I	1	1.36	–	−2.09	−0.16
Zn I	2	3.58	0.03	−0.98	0.07	Zn I	2	2.72	0.03	−1.83	0.10
Sr II	2	1.99	0.02	−0.88	0.17	Sr II	1	0.69	–	−2.18	−0.25
Y II	5	1.14	0.05	−1.07	−0.02	Y II	7	0.12	0.11	−2.09	−0.16
Zr I	0	–	–	–	–	Zr I	1	0.79	–	−1.79	0.14
Zr II	0	–	–	–	–	Zr II	1	0.68	–	−1.90	0.03
Ba II	2	1.31	0.07	−0.87	0.18	Ba II	2	0.22	0.02	−1.96	−0.03
La II	1	0.50	–	−0.60	0.45	La II	1	−0.68	–	−1.78	0.16
Ce II	2	0.37	0.03	−1.21	−0.16	Ce II	5	−0.39	0.18	−1.97	−0.04
Nd II	3	0.56	0.06	−0.86	0.19	Nd II	10	−0.36	0.04	−1.78	0.15
Eu II	1	−0.33	–	−0.85	0.20	Eu II	1	−1.06	–	−1.58	0.33

Table 7 – *continued*

Species	N	$\log\epsilon(X)$	σ	[X/H]	[X/Fe]	Species	N	$\log\epsilon(X)$	σ	[X/H]	[X/Fe]
		HD 141531						HD 142948			
C (CH)	2	6.33	0.20	−2.10	−0.48	C (CH)	2	7.72	0.20	−0.71	0.03
O I	2	7.33	0.01	−1.35	0.34	O I	2	8.43	0.02	−0.26	0.47
Na I	2	4.28	0.05	−1.96	−0.27	Na I	3	5.73	0.13	−0.51	0.22
Mg I	2	6.30	0.15	−1.29	0.40	Mg I	3	7.24	0.12	−0.36	0.38
Al I	2	4.74	0.10	−1.71	−0.02	Al I	4	5.94	0.08	−0.51	0.23
Si I	5	6.03	0.10	−1.48	0.21	Si I	5	7.07	0.05	−0.44	0.30
K I	1	3.99	–	−1.04	0.65	K I	1	5.04	–	0.01	0.75
Ca I	4	4.90	0.03	−1.44	0.25	Ca I	4	5.78	0.01	−0.56	0.18
Sc II	5	1.40	0.11	−1.75	−0.06	Sc II	5	2.57	0.12	−0.58	0.16
Ti I	4	3.33	0.07	−1.62	0.07	Ti I	4	4.44	0.09	−0.51	0.23
Ti II	4	3.71	0.08	−1.24	0.46	Ti II	3	4.40	0.21	−0.55	0.19
V I	4	2.10	0.07	−1.83	−0.13	V I	5	3.31	0.04	−0.62	0.12
Cr I	12	3.68	0.06	−1.96	−0.27	Cr I	13	4.67	0.15	−0.97	−0.23
Cr II	2	4.11	0.02	−1.53	0.16	Cr II	3	4.88	0.03	−0.76	−0.02
Mn I	3	3.29	0.04	−2.14	−0.45	Mn I	3	4.45	0.06	−0.98	−0.24
Fe I	54	5.81	0.06	−1.69	0.00	Fe I	61	6.76	0.10	−0.74	0.00
Fe II	13	5.86	0.03	−1.64	0.05	Fe II	13	6.75	0.06	−0.75	−0.02
Co I	3	3.22	0.12	−1.77	−0.08	Co I	3	4.36	0.11	−0.63	−0.13
Ni I	7	4.42	0.12	−1.80	−0.11	Ni I	5	5.62	0.04	−0.60	0.13
Cu I	1	1.60	–	−2.59	−0.90	Cu I	1	3.10	–	−1.09	−0.35
Zn I	2	2.80	0.04	−1.76	−0.07	Zn I	2	3.89	0.06	−0.67	0.07
Sr II	1	1.00	–	−1.87	−0.18	Sr II	1	1.89	–	−0.98	−0.24
Y II	6	0.27	0.13	−1.94	−0.24	Y II	6	1.33	0.32	−0.88	−0.14
Zr I	0	–	–	–	–	Zr I	0	–	–	–	–
Zr II	1	0.75	–	−1.83	−0.14	Zr II	0	–	–	–	–
Ba II	2	0.39	0.05	−1.79	−0.10	Ba II	2	1.17	0.01	−1.01	−0.27
La II	1	−0.56	–	−1.67	0.03	La II	1	0.56	–	−0.54	0.20
Ce II	4	−0.31	0.12	−1.89	−0.20	Ce II	3	0.54	0.20	−1.04	−0.30
Nd II	10	−0.20	0.08	−1.62	0.07	Nd II	6	0.79	0.10	−0.63	0.11
Eu II	1	−0.95	–	−1.47	0.22	Eu II	1	0.08	–	−1.55	0.14

Table 8. Programme star abundances.

Species	N	$\log\epsilon(X)$	σ	[X/H]	[X/Fe]	Species	N	$\log\epsilon(X)$	σ	[X/H]	[X/Fe]
		J221821−183424						C222531−145437			
C (CH)	2	6.55	0.20	−1.88	−0.30	C (CH)	2	7.15	0.20	−1.28	−0.05
O I	2	7.55	0.04	−1.13	0.45	O I	2	7.96	–	−0.73	0.49
Na I	1	4.75	–	−1.49	0.09	Na I	2	5.12	0.02	−1.12	0.10
Mg I	3	6.37	0.09	−1.23	0.35	Mg I	2	6.90	0.08	−0.70	0.53
Al I	1	5.08	–	−1.37	0.21	Al I	4	5.94	0.10	−0.51	0.71
Si I	5	6.32	0.08	−1.19	0.39	Si I	5	7.07	0.15	−0.44	0.79
K I	1	4.34	–	−0.69	0.89	K I	1	4.42	–	−0.61	0.62
Ca I	4	5.01	0.04	−1.33	0.25	Ca I	4	5.57	0.04	−0.77	0.45
Sc II	4	1.50	0.12	−1.65	−0.07	Sc II	4	2.08	0.13	−1.07	0.16
Ti I	0	–	–	–	–	Ti I	4	4.10	0.03	−0.85	0.37
Ti II	4	3.80	0.13	−1.15	0.43	Ti II	2	4.12	0.13	−0.83	0.40
V I	3	2.28	0.01	−1.65	−0.07	V I	5	2.91	0.10	−1.01	0.22
Cr I	11	3.80	0.06	−1.84	−0.26	Cr I	8	4.24	0.17	−1.40	−0.17
Cr II	2	4.07	0.03	−1.57	0.01	Cr II	1	4.38	–	−1.26	−0.03
Mn I	2	3.38	0.03	−2.05	−0.46	Mn I	3	3.98	0.05	−1.45	−0.23
Fe I	52	5.92	0.09	−1.58	0.00	Fe I	60	6.27	0.10	−1.23	0.00
Fe II	13	5.94	0.05	−1.56	0.02	Fe II	10	6.30	0.06	−1.20	0.03
Co I	1	3.32	–	−1.67	−0.09	Co I	4	3.77	0.09	−1.22	0.00
Ni I	5	4.61	0.14	−1.61	−0.03	Ni I	7	5.07	0.09	−1.15	0.08
Cu I	1	1.81	–	−2.38	−0.80	Cu I	1	2.72	–	−1.47	−0.24
Zn I	1	3.07	–	−1.49	0.09	Zn I	2	3.56	0.24	−1.00	0.23
Sr II	1	1.39	–	−1.48	0.10	Sr II	1	:1.99	–	:−0.88	:0.35
Y II	3	0.44	0.02	−1.77	−0.19	Y II	5	1.78	0.16	−0.43	0.79

Table 8 – *continued*

Species	N	$\log\epsilon(X)$	σ	[X/H]	[X/Fe]	Species	N	$\log\epsilon(X)$	σ	[X/H]	[X/Fe]
Zr I	0	–	–	–	–	Zr I	3	2.07	0.05	−0.51	0.72
Zr II	1	0.97	–	−1.61	−0.03	Zr II	0	–	–	–	–
Ba II	1	0.60	–	−1.58	0.00	Ba II	2	1.58	0.01	−0.60	0.62
La II	1	−0.58	–	−1.67	−0.09	La II	2	0.51	0.02	−0.59	0.64
Ce II	3	−0.39	0.06	−1.97	−0.39	Ce II	5	0.73	0.15	−0.85	0.37
Nd II	10	−0.22	0.07	−1.64	−0.06	Nd II	8	0.88	0.13	−0.54	0.69
Eu II	1	−0.86	0.11	−1.38	0.20	Eu II	1	−0.29	–	−0.81	0.42
		J223504−152834						J223811−104126			
C (CH)	2	7.71	0.30	−0.72	−0.10	C (CH)	2	7.05	0.25	−1.38	0.05
O I	2	8.50	0.10	−0.19	0.43	O I[a]	3	7.41	0.13	−1.28	0.15
Na I	3	5.87	0.12	−0.37	0.26	Na I	1	4.89	–	−1.35	0.08
Mg I	3	7.48	0.15	−0.12	0.51	Mg I	2	6.51	0.03	−1.09	0.34
Al I	3	6.12	0.09	−0.33	0.29	Al I	2	5.13	0.13	−1.32	0.11
Si I	5	7.24	0.10	−0.27	0.35	Si I	3	6.42	0.04	−1.09	0.34
K I	1	5.05	–	0.02	0.64	K I	1	4.50	–	−0.53	0.90
Ca I	4	6.06	0.03	−0.28	0.34	Ca I	4	5.32	0.03	−1.02	0.41
Sc II	5	2.65	0.10	−0.50	0.13	Sc II	2	1.60	0.03	−1.55	−0.12
Ti I	4	4.65	0.02	−0.30	0.32	Ti I	0	–	–	–	–
Ti II	1	4.67	–	−0.28	0.34	Ti II	4	3.79	0.09	−1.16	0.27
V I	4	3.50	0.11	−0.43	0.19	V I	1	2.45	–	−1.48	−0.05
Cr I	7	4.90	0.11	−0.74	−0.11	Cr I	12	4.10	0.06	−1.54	−0.11
Cr II	2	4.84	0.04	−0.79	−0.17	Cr II	3	4.34	0.07	−1.30	0.12
Mn I	3	4.66	0.04	−0.77	−0.15	Mn I	2	3.50	0.01	−1.93	−0.51
Fe I	63	6.88	0.12	−0.62	0.00	Fe I	33	6.07	0.06	−1.43	0.00
Fe II	12	6.87	0.07	−0.63	−0.01	Fe II	9	6.04	0.07	−1.46	−0.03
Co I	3	4.39	0.09	−0.60	0.02	Co I	0	–	–	–	–
Ni I	7	5.64	0.09	−0.58	0.05	Ni I	2	4.84	0.04	−1.38	0.05
Cu I	1	3.72	–	−0.47	0.15	Cu I	1	1.96	–	−2.23	−0.80
Zn I	2	4.21	0.03	−0.35	0.27	Zn I	2	3.15	0.05	−1.41	0.02
Sr II	1	:2.25	–	:−0.62	:0.00	Sr II	1	1.64	–	−1.23	0.20
Y II	3	1.80	0.03	−0.41	0.21	Y II	6	0.76	0.06	−1.45	−0.02
Zr I	3	2.26	0.05	−0.32	0.31	Zr I	0	–	–	–	–
Zr II	0	–	–	–	–	Zr II	0	–	–	–	–
Ba II	2	1.65	0.02	−0.53	0.10	Ba II	2	0.78	0.07	−1.40	0.03
La II	1	0.76	–	−0.34	0.28	La II	0	–	–	–	–
Ce II	3	0.87	0.13	−0.71	−0.09	Ce II	2	−0.07	0.02	−1.65	−0.22
Nd II	6	1.27	0.13	−0.15	0.47	Nd II	1	−0.25	–	−1.67	−0.24
Eu II	1	0.40	–	−0.12	0.50	Eu II	1	−0.55	–	−1.07	0.36
		C2306265−085103									
C (CH)	2	7.20	0.20	−1.23	−0.10						
O I	2	8.02	0.04	−0.67	0.46						
Na I	2	5.31	0.01	−0.93	0.21						
Mg I	2	6.90	0.06	−0.70	0.44						
Al I	4	5.65	0.08	−0.80	0.33						
Si I	5	6.78	0.08	−0.73	0.40						
K I	1	4.46	–	−0.57	0.56						
Ca I	4	5.56	0.04	−0.78	0.35						
Sc II	3	2.15	0.09	−1.00	0.13						
Ti I	4	4.13	0.03	−0.82	0.32						
Ti II	3	4.32	0.35	−0.63	0.51						
V I	4	2.85	0.06	−1.09	0.05						
Cr I	3	4.13	0.12	−1.51	−0.38						
Cr II	1	4.50	–	−1.14	−0.01						
Mn I	3	4.10	0.05	−1.33	−0.20						
Fe I	62	6.37	0.12	−1.13	0.00						
Fe II	11	6.39	0.10	−1.11	0.02						
Co I	3	3.88	0.06	−1.11	0.02						
Ni I	7	5.11	0.07	−1.11	0.02						
Cu I	1	2.96	–	−1.23	−0.10						
Zn I	2	3.48	0.15	−1.08	0.05						
Sr II	1	1.74	–	−1.13	0.00						

Table 8 – *continued*

Species	N	$\log\epsilon(X)$	σ	[X/H]	[X/Fe]	Species	N	$\log\epsilon(X)$	σ	[X/H]	[X/Fe]
Y II	4	1.26	0.26	−0.95	0.18						
Zr I	3	1.60	0.05	−0.98	0.16						
Zr II	0	–	–	–	–						
Ba II	2	0.95	0.10	−1.23	−0.10						
La II	1	0.07	–	−1.03	0.10						
Ce II	2	0.09	0.02	−1.49	−0.36						
Nd II	7	0.58	0.21	−0.84	0.29						
Eu II	1	−0.41	–	−0.93	0.20						

[a]Abundance derived from the permitted O I triplet instead of the forbidden [O I] lines, see Section 4.3.

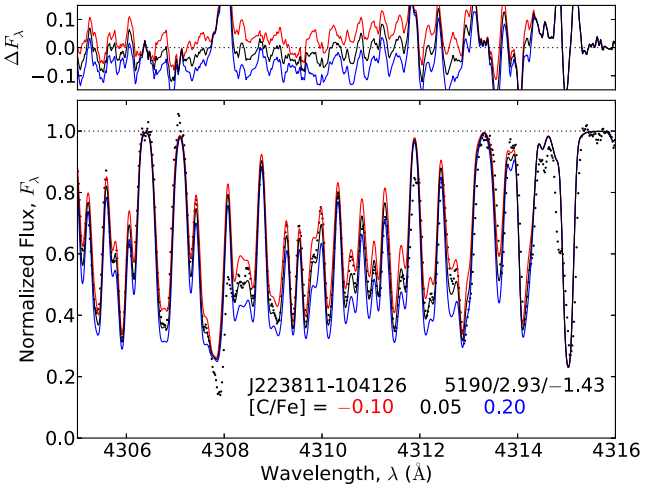

Figure 5. The carbon CH feature near 4313 Å in programme star J223811−104126. The best-fitting synthetic spectra is shown, with synthetic spectra for ±0.15 dex about the best-fitting abundance.

4.1 Carbon

Carbon is produced by the triple-α process and ejected through supernovae (SNe) events, or by mass-loss from asymptotic giant branch (AGB) stars (Kobayashi, Karakas & Umeda 2011).

We have measured carbon abundances for all stars from the *G* band head near 4313 Å and the CH molecular feature at 4323 Å, by comparing observed spectra with synthetic spectra for different carbon abundances. The synthetic spectra were convolved with a Gaussian kernel where the width was determined from nearby atomic lines with known abundances. Carbon was measured separately for both features, and in all stars the two measurements agree within 0.10 dex. An example fit to this spectral region for J223811−104126 is shown in Fig. 5.

Carbon abundances in our standard stars agree well with the literature. For HD 136316 we find [C/Fe] = −0.50 ± 0.15, where Gratton et al. (2000) find [C/Fe] = −0.66. Our [C/Fe] = −0.48 measurement for HD 141531 agrees with Gratton et al. (2000) to within 0.06 dex. Most programme stars have near-solar carbon abundances, ranging from [C/Fe] = −0.30 for J221821−183424, and +0.05 for J223811−104126.

4.2 Sodium and aluminium

Our line list includes three clean, unblended sodium lines at λλ5688, 6154, and 6161. Not all three of these lines were detectable in each star. In the hottest and most metal-poor stars, J223811−104126 and J221821−183424, respectively, only the λ5688 line was measurable. For stars where multiple sodium lines were available, the line-to-line scatter is usually around 0.04 dex with a maximum of 0.09 dex in HD 41667. However, in calculating total abundance uncertainties (see Section 4.6) we have conservatively assumed a minimum random scatter of ±0.10 dex for all stars.

Our [Na/Fe] abundances appear systematically higher than values found in the literature by ∼0.10 dex. For HD 142948 we find [Na/Fe] = 0.22, which is +0.10 dex higher than that found by Gratton et al. (2000), and similarly we find HD 76932 to be +0.10 dex higher than reported by Fulbright (2000). Gratton et al. (2000) also found HD 136316 to have [Na/Fe] = −0.29, where we find [Na/Fe] = −0.14, yet excellent agreement is found in the stellar parameters in Gratton et al. (2000) and this study. Different solar compositions employed between this study and earlier work can account for ∼0.08 dex of this effect, leaving the residual difference well within the observational uncertainties. However, it is important to note that the [Na/Fe] abundance ratios presented in this study may be slightly higher compared to previous studies. While a systematic offset may be present, no intrinsic abundance dispersion in [Na/Fe] is present in the Aquarius sample.

There are six aluminium transitions in our optical spectra. The strongest of these lines occur at λ3944 and 3961 and are visible in all of our stars. However this is a particularly crowded spectral region: the lines fall between the strong Ca H and K lines, with the λ3961 transition clearly located in the wing of the Ca H line. Additionally, the λλ3944 and 3961 lines have appreciable departures from the assumption of local thermodynamic equilibrium (LTE), resulting in underestimated abundances by up to ∼0.6 dex (Baumueller & Gehren 1997). Instead, we have measured Al abundances from other available transitions: the Al I lines at λλ6696, 6698, 7835 and 7836. Generally, the four Al I lines are in reasonable agreement with one another, yielding random scatter of less than 0.05 dex.

4.3 α-elements (O, Mg, Si, Ca and Ti)

The α-elements (O, Mg, Si, Ca and Ti) are forged through α-particle capture during hydrostatic burning of carbon, neon and silicon. Material enriched in α-elements is eventually dispersed into the interstellar medium following Type II core-collapse SNe.

Oxygen can be a particularly difficult element to measure. There are only a handful of lines available in an optical spectrum: the forbidden [O I] lines at λλ6300 and 6363 and the O I triplet lines at ∼7775 Å. The forbidden lines are very weak and become difficult to measure in hot and/or metal-poor stars ([Fe/H] $\lesssim$ −1.5 dex). When they are present, depending on the radial velocity of the star, the [O I] lines can be significantly affected by telluric absorption. The λ6363 line is intrinsically weak, blended with CN, and it falls in the wing of a strong Ca I auto-ionization feature. Because

of these properties it is rarely used in abundance studies. Moreover, the λ6300 line is blended with a Ni I absorption line (Allende Prieto, Lambert & Asplund 2001). Hence the region requires careful consideration. Although the O I triplet lines at ∼7775 Å are stronger than the forbidden lines, they are extremely susceptible to non-LTE effects, surface granulation (Asplund & García Pérez 2001), and are sensitive to changes in microturbulence. Our forbidden [O I] abundances for HD 136316 agree well with those from Gratton et al. (2000) – the difference is only 0.07 dex.

The [O I] lines were measurable in four of our Aquarius stream candidates. The λ6300 line in one of our candidates, C2306265−085103, was sufficiently affected by telluric absorption such that we deemed the line unrecoverable. Thus, only the λ6363 transition was used to derive an oxygen abundance for C2306265−085103. In our hottest star, J223811−104126, the forbidden oxygen lines were not detected above a 3σ significance. After synthesizing the region, we deduce a very conservative upper limit of [O/Fe] < 0.50 from the [O I] lines. This is consistent with the rest of our candidates, with [O/Fe] abundances varying between 0.43 and 0.49 dex.

In order to derive an oxygen measurement for J223811−104126, we were forced to use the triplet lines at ∼7775 Å. We extended these measurements for all Aquarius stars, and a mean abundance for each candidate was found from the synthesis of the permitted triplet lines. Oxygen abundances inferred from the triplet lines in all other stars were systematically ∼+0.3 dex higher than abundances calculated from the [O I] forbidden lines. García Pérez et al. (2006) found the same result from stars with similar stellar parameters: [O/Fe] values based on the O I permitted triplet lines are on average $+0.19 \pm 0.07$ dex higher than those found from the forbidden lines, which did not include non-LTE corrections of +0.08 dex. Thus, we attribute our ∼+0.3 dex offset between measurements of the [O I] and O I triplet lines to non-LTE and 3D effects. García Pérez et al. (2006) concluded that the forbidden lines, when not too weak, probably give the most reliable estimate of oxygen abundance. From the permitted O I triplet in J223811−104126, we derive an oxygen abundance of [O/Fe] $= 0.42 \pm 0.01$ dex (random scatter). This measurement will be systematically higher than the 'true' abundance if it were discernible from the [O I] lines, of the order of ∼+ 0.3 dex. When we apply this crude offset derived from the rest of our sample, we arrive at a corrected abundance of [O/Fe] $= 0.15 \pm 0.13$ (total uncertainty) for J223811−104126. This is the most oxygen-deficient star in our sample by a factor of 2.

Depending on the radial velocity of the star, some magnesium lines were affected by telluric absorption, particularly the λλ6318 and 6965 transitions. Atmospheric absorption was most notable for C222531−145437, where three of the four Mg transitions in our line list suffered some degree of telluric absorption, requiring an attentive correction. Every amended absorption profile was carefully examined, and lines with suspicious profiles were excluded from the final magnesium abundance. All [α/Fe] abundance ratios in the standard stars are in excellent agreement with the literature. Typically, the difference is 0.01 dex, with the largest discrepancy of Δ[Ti/Fe] = +0.13 dex for HD 76932 when compared with Fulbright (2000).

While Wylie-de Boer et al. (2012) find almost no scatter (±0.02 dex) in [Mg/Fe] for stars common to both studies, we find C222531−145437 and J223504−152834 to be almost +0.20 dex higher than the rest of the sample. Of the Mg I line profiles measured, only two transitions are common to both line lists: λλ6318 and 6319. The oscillator strengths differ between studies; in these two lines the log *gf* differs by −0.24 and −0.27 dex, respectively (our oscillator strengths are lower). This indicates that the difference in oscillator strengths may explain the ∼0.2 dex offset in [Mg/Fe] between this study and Wylie-de Boer et al. (2012).

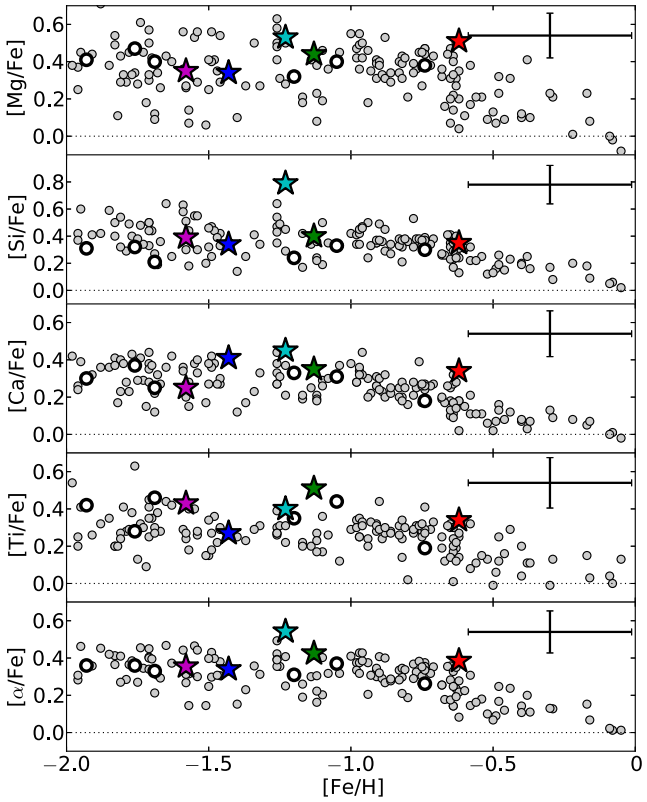

Figure 6. α-element abundances with respect to iron content. The mean [α/Fe] abundance from these is shown in the bottom panel. The solar element-to-iron ratio is marked as a dotted line in each panel. Colours are as per Fig. 3. Standard stars are shown as open circles. Mean conservative *total uncertainties* (random and systematic) for stars in this study are shown in each panel. The filled circles represent Milky Way field stars from Fulbright (2000). Oxygen abundances are shown separately in Fig. 10.

Of all the α-elements, calcium has the smallest measurement scatter in our stars. The mean was formed from four line measurements in each star, with a typical random scatter of 0.01 dex. Nevertheless, the aforementioned conservative minimum of 0.10 dex for random scatter applies, and uncertainties in stellar parameters will contribute to the total error budget. As shown in Fig. 6, all Aquarius stream candidates show super-solar [Ca/Fe], ranging between +0.23 and +0.43 dex, consistent with [(Mg,Si,Ti)/Fe] measurements.

C222531−145437 has an unusually high silicon abundance ([Si/Fe] = 0.79), well outside the uncertainties of the rest of our sample. The 5 silicon line abundances in this star are in relatively good agreement with each another. If we exclude the highest measurement, then the mean abundance drops only slightly to [Si/Fe] $= 0.73 \pm 0.04$ (random scatter). The lowest silicon line abundance for C222531−145437 is [Si/Fe] = 0.61, which is still significantly higher than the mean abundance for any other star. With [Si/Fe] = +0.79, star C222531−145437 lies above the majority of field stars. Examination of Fig. 6 would indicate that for all other α-elements, it remains near the upper envelope defined by the field stars. It is not obvious why this is the case.

Titanium abundance ratios for the stream show typical levels of α-enhancement. Our mean titanium abundances are derived from four to seven clean unblended Ti I and Ti II lines. In our hottest and

most metal-poor stars the mean Ti abundance is found from only Ti II lines, as no suitable Ti I transitions were available.

4.4 Iron-peak elements

The Fe-peak elements (Sc to Zn) are primarily synthesized by the explosive nucleosynthesis of oxygen, neon, and silicon burning. Ignition can occur from Type II SN explosions of massive stars, or once a white dwarf accretes enough material to exceed the Chandrasekhar mass limit and spontaneously ignite carbon, leading to a Type Ia SN.

Although not all Fe-peak elements are created equally, many Fe-peak elements generally exhibit similar trends with overall metallicity. All exhibit a positive trend with increasing iron abundance, with varying gradients.

The [Sc/Fe] measurements presented in Fig. 7 are averaged from six clean Sc II lines, and there is very little line-to-line scatter, the largest of which is 0.06 dex. The number of clean, suitable Cr I lines available between members fluctuated from three to twelve. Very little line-to-line scatter is present in both Cr I and Cr II: the random scatter is below 0.04 dex for most stars. Chromium abundances are only available for one of the standard stars, where our [Cr/Fe] = 0.03 is in excellent agreement with Fulbright (2000), where they find [Cr/Fe] = 0.04.

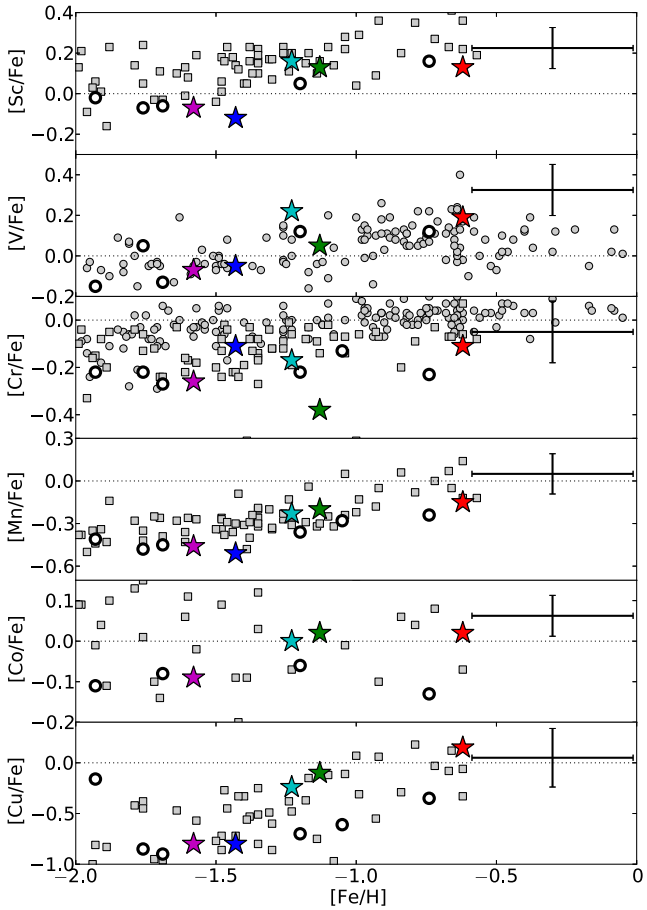

Figure 7. Iron-peak element abundances (Sc, V, Cr, Mn, Co and Cu) with respect to iron for all Aquarius stream stars. Ni, an additional Fe-peak element, is discussed in Section 5.5 and shown in Fig. 12. Colours are as per Fig. 3. Standard stars are shown as open circles. Mean conservative *total uncertainties* (random and systematic) for this study are shown in each panel. Filled circles and squares represent Milky Way field stars from Fulbright (2000) and Ishigaki, Aoki & Chiba (2013), respectively. Unlike Fig. 6, panels have different *y*-axis ranges to accommodate the data.

Manganese demonstrates a strong trend with increasing iron abundance (Fig. 7). A significant source of Mn comes from Type Ia SN, and the strong [Mn/Fe]–[Fe/H] correlation is consistent with chemodynamical simulations (Kobayashi & Nakasato 2011), as well as thick disc observations by Reddy, Lambert & Allende Prieto (2006). Although Mn is known to demonstrate significant departures from LTE, we have not applied any non-LTE corrections to our abundances.

Abundances of Co I lines were calculated by synthesis, as they demonstrate appreciable broadening due to hyperfine structure. Although they are known to suffer significant departures from LTE (Bergemann, Pickering & Gehren 2010), no corrections have been made for these data. In general, [Co/H] follows [Fe/H] in our candidates.

Most Aquarius stream stars have seven clean Ni I transitions available. These lines are in excellent agreement, with a typical scatter of 0.03 dex. Nickel abundances have been published for two of our standard stars: HD 76932 (Fulbright 2000) and HD 141531 (Shetrone 1996). In both cases, our [Ni/Fe] abundance ratios are slightly higher by +0.08 and +0.10 dex, respectively. The different solar compositions employed by these studies can only account for 0.01 dex of this discrepancy, and the differences in oscillator strengths for common Ni I lines are negligible. Overall, the [Ni/Fe] abundance ratios in the Aquarius stream stars do not deviate greatly from the solar ratio.

Hyperfine structure data has been included for the synthesis of Cu abundances. The offsets between EW and synthesis abundances for Cu were significant: ∼0.4 dex higher for some stars without the inclusion of hyperfine structure information. Cu abundances have also been determined by synthesis, and are consistent with the Milky Way trend.

4.5 Neutron-capture elements

Neutron-capture elements (Sr to Eu; $38 \leq Z \leq 63$) can be forged through multiple nucleosynthetic processes. The two primary processes that produce these elements are the rapid (*r*)-process and the slow (*s*)-process. While the *r*-process is theorized to occur in SN explosions, the *s*-process takes place foremost in AGB stars with a significant contribution from massive stars at higher metallicities (e.g. Meyer 1994), although models of rotating massive stars may change this picture at the very lowest metallicities (Frischknecht, Hirschi & Thielemann 2012).

4.5.1 Strontium, yttrium and zirconium

These neutron-capture elements belong to the first *s*-process peak, and generally increase in lock-step with each another. [Y II/Fe] and [Zr I, Zr II/Fe] are in good agreement among all candidates. Strontium was measured by synthesis of the λλ4077 and 4215 lines. Although these lines are strong, they are often blended by a wealth of unresolved atomic and molecular features.

The Aquarius stream candidates have Y abundances consistent with halo field stars, with the exception of C222531−145437. With [Y/Fe] = 0.79, C222531−145437 is significantly overabundant in Y for its metallicity (see fig. 4 of Travaglio et al. 2004). C222531−145437 is consistently overabundant in Zr, too. All other programme and standard stars have first *n*-capture peak abundances

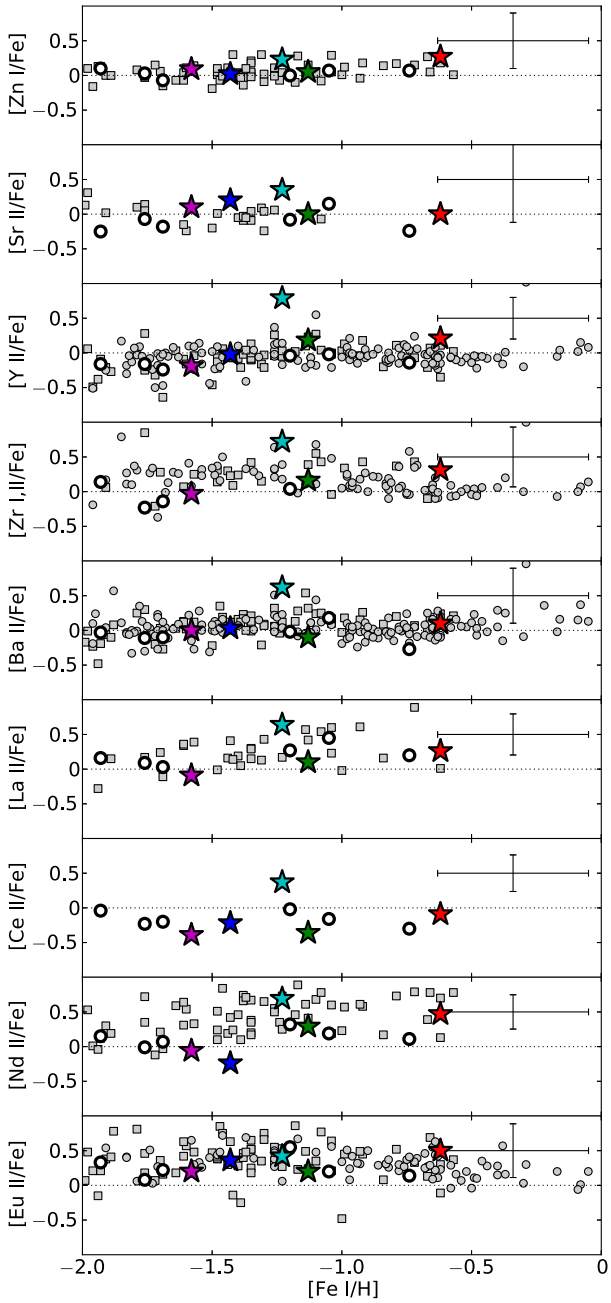

Figure 8. Element ratios for Aquarius stream stars. In the case of [Zr/Fe], [Zr I/Fe] is taken where available and [Zr II/Fe] if no measurement was available for Zr I. See Table 8 for details. Standard stars are shown as open circles. Mean conservative *total uncertainties* (random and systematic) for this study are shown in each panel. Filled circles and squares represent Milky Way field stars from Fulbright (2000) and Ishigaki et al. (2013), respectively. Panels have varying *y*-axis ranges to accommodate the data.

and trends that are consistent with the chemical evolution of the Milky Way (Fig. 8).

4.5.2 *Barium and lanthanum*

Barium and lanthanum belong to the second *s*-process peak. Ba has appreciable hyperfine and isotopic splitting, and its measurement requires some careful consideration. Solar Ba isotopic ratios have been adopted. Our standard stars have [Ba/Fe] abundances typical of the Milky Way halo. Two standard stars have existing [Ba/Fe] measurements from high-resolution spectra: HD 44007 and HD 76932. We find HD 44007 to have [Ba/Fe] = 0.03, which is in good agreement with Burris et al. (2000), who find 0.05 dex. For HD 76932 our measurement of [Ba/Fe] = 0.18 is in reasonable agreement with the Fulbright (2000) value of −0.02 dex, especially when differences in adopted solar composition are considered.

With one exception, the Aquarius stream candidates have [Ba/Fe] abundance ratios that are indistinguishable from field stars, ranging between [Ba/Fe] = −0.10 to 0.10 dex. The exception is C222531−145437, the same star showing enhancements in Y and Zr, which has an anomalously high barium abundance of [Ba/Fe] = 0.62. This is ∼0.60 dex higher than the Milky Way trend at its given metallicity of [Fe/H] = −1.26 (Ishigaki et al. 2013). Our two Ba II lines in C222531−145437 are in excellent agreement with each other: [Ba/Fe] = 0.63, and 0.61.

Lanthanum abundances have been determined by synthesis of the λλ4558 and 5805 lines with hyperfine splitting data included. All stars have La abundances that are consistent with the chemical enrichment of the Galaxy (Ishigaki et al. 2013), with the exception of the Ba-rich star C222531−145437, where [La/Fe] = 0.64 is observed.

4.5.3 *Cerium, neodymium and europium*

Europium is primarily produced by the *r*-process, whereas the production of Ce and Nd is split between *s*- and *r*-process. Europium abundances have been determined by synthesizing the λ6645 Eu II transition with hyperfine splitting data from Kurucz & Bell (1995).

We chose not to use the λ6437 Eu II line as it is appreciably blended by a nearby Si I line (Lawler et al. 2001a), and our measurements were consistent with a hidden blend: the λ6437 Eu II abundance was systematically higher than the λ6645 counterpart. One Aquarius stream candidate, C222531−145437, appears enhanced in all [*s*-process/Fe] abundance ratios compared to the programme and standard sample. However no noteworthy difference in Eu, which is generally considered to be a *r*-process dominated element, was observed.

4.6 Uncertainties in chemical abundances

The uncertainties in chemical abundances are primarily driven by systematic uncertainties in stellar parameters, with a small contribution of random measurement scatter from individual lines. In order to calculate the abundance uncertainties due to stellar parameters, we have independently varied the stellar parameters by the adopted uncertainties, and measured the resultant change in chemical abundances. For lines requiring synthesis due to hyperfine structure, the difference in chemical abundances has been calculated from EWs. However, the effect of wing broadening due to hyperfine or isotopic splitting was generally small.

The individual abundance errors from varying each of the stellar parameters were added in quadrature to obtain the systematic error. To obtain the total error, we added in quadrature the systematic error with the standard error of the mean (random error). In some cases, the standard error about the mean is unrealistically small. As discussed earlier in Section 4.2, we have conservatively adopted an abundance floor of 0.10 dex for the standard deviation (i.e. max (0.10, $\sigma(\log_\epsilon X)$). These resultant changes in abundances and total uncertainties are listed for all stars in Table 9. These total uncertainties have been used in all figures. This provides us with

Table 9. Abundance uncertainties due to errors in stellar parameters.

					Total uncertainty	
Species	$T_{\rm eff}+125$ K Δabund.	$\log g+0.20$ dex Δabund.	$\xi_t+0.30\,{\rm km\,s^{-1}}$ Δabund.	$\max(0.10,\sigma)/\sqrt{(N)}$ (dex)	[X/H] (dex)	[X/Fe] (dex)
HD 41667						
O I	0.03	0.08	−0.01	0.07	0.11	0.16
Na I	0.13	0.00	−0.02	0.10	0.16	0.21
Mg I	0.08	0.01	−0.01	0.05	0.10	0.18
Al I	0.10	0.01	−0.01	0.06	0.11	0.18
Si I	0.02	0.03	−0.02	0.04	0.06	0.16
K I	0.14	−0.03	−0.17	0.10	0.24	0.28
Ca I	0.13	−0.01	−0.10	0.05	0.17	0.22
Sc II	−0.03	0.08	−0.08	0.05	0.13	0.18
Ti I	0.22	0.01	−0.01	0.05	0.22	0.25
Ti II	−0.04	0.07	−0.15	0.14	0.23	0.27
V I	0.25	0.01	−0.03	0.05	0.26	0.28
Cr I	0.23	0.00	−0.20	0.03	0.31	0.33
Cr II	−0.07	0.08	−0.06	0.07	0.14	0.20
Mn I	0.17	0.01	−0.07	0.06	0.19	0.23
Fe I	0.16	0.01	−0.07	0.02	0.17	–
Fe II	−0.10	0.08	−0.04	0.03	0.14	–
Co I	0.18	0.03	−0.01	0.04	0.19	0.22
Ni I	0.12	0.03	−0.01	0.05	0.13	0.18
Cu I	0.19	0.03	−0.16	0.10	0.27	0.29
Zn I	−0.03	0.06	−0.09	0.07	0.14	0.20
Sr II	0.24	0.01	−0.06	0.10	0.27	0.29
Y II	0.00	0.08	−0.09	0.09	0.15	0.19
Zr I	0.27	0.01	0.00	0.07	0.28	0.30
Zr II	0.00	0.08	−0.01	0.10	0.13	0.18
Ba II	0.01	0.06	−0.21	0.07	0.23	0.26
La II	0.01	0.07	−0.02	0.07	0.10	0.16
Ce II	0.04	0.08	−0.04	0.09	0.13	0.17
Nd II	0.02	0.06	−0.07	0.03	0.10	0.16
Eu II	−0.05	0.04	−0.06	0.10	0.13	0.20

Table 9 is published for all standard and programme stars in the electronic edition. A portion is shown here for guidance regarding its form and content.

an uncertainty for all abundances, in all stars, of [X/H]. Generally though, we are most interested in the uncertainty in [X/Fe]. In order to calculate this uncertainty, the correlations in uncertainties due to stellar parameters between (X, Fe) need to be considered. We have followed the description in Johnson (2002) to calculate these correlations, and the overall uncertainties in [X/Fe], which are listed in Table 9 for all programme and standard stars.

5 DISCUSSION

5.1 Stellar parameter discrepancies with Wylie-de Boer et al. (2012)

We now seek to investigate the nature of the Aquarius stream and in particular, the globular cluster origin suggested by Wylie-de Boer et al. (2012). Before proceeding, we now compare our stellar parameters with those of Wylie-de Boer et al. (2012) for the four stars in common. Wylie-de Boer et al. (2012) deduce their stellar parameters ($T_{\rm eff}$, $\log g$, ξ_t, [M/H]) by minimizing the χ^2 difference between the observed spectra and synthetic spectra from the Munari et al. (2005) spectral library. For the four stars common to both samples, the stellar parameters reported in Wylie-de Boer et al. (2012) differ from our values listed in Table 3. In general, effective temperatures between the two studies agree within the uncertainties. The only aberration is J223811−104126, where we find an effective temperature of 5190 K, ∼450 K cooler than the 5646 K found by Wylie-de Boer et al. (2012). Similarly, Williams et al. (2011) report a hotter effective temperature of 5502 K from low-resolution spectra. This is the largest discrepancy we find in any of our standard or programme stars.

Photometric temperature relationships support our spectroscopic temperature for J223811−104126. The Ramírez & Meléndez (2005) relationship for giants suggests an effective temperature of 5240 K, which is 50 K warmer than our spectroscopically derived temperature. Furthermore, the metallicity-independent $J-K$ colour–$T_{\rm eff}$ relationship for giants by Alonso, Arribas & Martínez-Roger (1999) yields an effective temperature of 5215 K, 25 K warmer than our spectroscopic temperature. As a test, we set the temperature for J223811−104126 to be 5600 K – within the temperature regime reported by Williams et al. (2011) and Wylie-de Boer et al. (2012). The slopes and offsets in abundance with excitation potential and REW were large: $m_{\rm Fe\,I}=-0.099$ dex eV^{-1}, 0.162 dex, $m_{\rm FeII}=-0.133$ dex eV^{-1}, −0.033 dex, respectively, and in doing so we could not find a representative solution for this temperature.

Williams et al. (2011) and Wylie-de Boer et al. (2012) find J223811−104126 to be a subgiant/dwarf, with a surface gravity $\log g=4.16$ and 4.60, respectively. We note that the Williams et al. (2011) and Wylie-de Boer et al. (2012) effective temperatures for J223811−104126 are 150–300 K hotter than the Casagrande et al. (2010) $J-K$ photometric temperature calibration for dwarfs and

subgiants. We find the surface gravity for J223811−104126 to be $\log g = 2.93 \pm 0.30$ dex, placing this star at the base of the red giant branch.

With the exception of J223811−104126, our surface gravities are largely in agreement with Wylie-de Boer et al. (2012). The only other noteworthy difference is for J221821−183424, where we find a lower gravity of $\log g = 0.88 \pm 0.30$ and Wylie-de Boer et al. (2012) find $\log g = 1.45 \pm 0.35$. Given the difference in the S/N between these studies, this difference is not too concerning. Wylie-de Boer et al. (2012) calculate the microturbulence from empirical relationships derived by Reddy et al. (2003) for dwarfs and Fulbright (2000) for giants. These relationships are based on the effective temperature and surface gravity. Our published microturbulent velocities agree excellently with the values presented in Wylie-de Boer et al. (2012), again with the exception of J223811−104126, where the difference in v_t is directly attributable to the offsets in other observables.

Of all the stellar parameters, metallicities exhibit the largest discrepancy between the two studies. In the Wylie-de Boer et al. (2012) study, after the stellar parameters ($T_{\rm eff}$, $\log g$, v_t, and an initial [M/H] estimate) were determined through a χ^2 minimization, the authors synthesized individual Fe I and Fe II lines using MOOG. Castelli & Kurucz (2003) stellar atmosphere models were employed (Freeman, private communication) – the same ones used in this study – albeit the interpolation schemes will have subtle differences. The median abundance of synthesized Fe I lines was adopted as the overall stellar metallicity, and scaled relative to the Sun using the Grevesse & Sauval (1998) solar composition.

The study of Wylie-de Boer et al. (2012) is of slightly lower resolution ($\mathcal{R} = 25\,000$ compared to $\mathcal{R} = 28\,000$ presented here), but with a much lower S/N: $\sim$25 pixel^{-1} compared to $>$100 pixel^{-1} achieved here. The line list employed in the Wylie-de Boer et al. (2012) utilized astrophysical oscillator derived from a reverse solar analysis on the solar spectrum. However, there are very few transitions listed in their line list: a maximum of 14 Fe I lines and 3 Fe II lines were available. For contrast, our analysis is based on 63 Fe I and 13 Fe II clean, unblended lines.

We first suspected that the discrepancy in derived metallicities could be primarily attributed to the difference in line lists. In order to test this hypothesis, we re-analysed our data using the Wylie-de Boer et al. (2012) line list and their stellar parameters. Excitation or ionization equilibria could not be achieved using any stellar parameters from Wylie-de Boer et al. (2012) within their quoted uncertainties. We find different metallicities for each star in common with differences up to 0.42 dex. Alternatively, if the Wylie-de Boer et al. (2012) line list is employed and we solve for stellar parameters (see Section 3.4), we obtain stellar parameters closer to *our* existing measurements tabulated in Table 3, which are also distinct from the Wylie-de Boer et al. (2012) values. From the four stars common between these studies, using the Wylie-de Boer et al. (2012) line list and our stellar parameters,[4] we observe a metallicity dispersion of $\sigma([{\rm Fe/H}]) = 0.32$ dex. This is contrast to the $\sigma([{\rm Fe/H}]) = 0.10$ dex reported by Wylie-de Boer et al. (2012) from six Aquarius stream stars. The discrepancy might be explainable by different methods of determining stellar parameters (e.g. χ^2-minimization compared to excitation and ionization equilibria), as well as the difference in quality of the spectra between these two studies.

[4] Here we are referring to a separate test in which we found the stellar parameters by excitation and ionization equilibria using the Wylie-de Boer et al. (2012) line list, *not* those listed in Table 3.

We note that given the small numbers of Fe lines used by Wylie-de Boer et al. (2012), even subtle changes to the stellar parameters produced large variations to both the individual and mean Fe abundances. Furthermore, one Fe I transition at λ6420 in the Wylie-de Boer et al. (2012) line list was either not detected at the 3σ level – even though the S/N at this point exceeds 115 pixel^{-1} in every observation – or it was blended with a stronger neighbouring transition.

5.2 The Aquarius stream metallicity distribution

Given the overall data quality and the limited Fe line list used for analysis, it appears the Aquarius stream stars conspired to present a tight metallicity distribution of $\sigma([{\rm Fe/H}]) = 0.10$ dex in the Wylie-de Boer et al. (2012) analysis (in our analysis we find $\sigma([{\rm Fe/H}]) = 0.33$ dex). When viewed in light of enhanced [Ni/Fe] and [Na/Fe] abundance ratios, Wylie-de Boer et al. (2012) interpreted this chemistry as a signature of a globular cluster origin for the Aquarius stream. Our study of high-resolution spectra with high S/N reveals a much broader metallicity distribution for the stream than previously reported. With just 5 stars we find the metallicity varies from [Fe/H] = −0.63 to −1.58. Although this is a small sample, we find the mean abundance and standard deviation to be [Fe/H] = -1.20 ± 0.33.

If the metallicity dispersion were smaller, as found by Wylie-de Boer et al. (2012), a globular cluster scenario may be plausible. Classical globular clusters typically exhibit very little dispersion in metallicity. An intrinsic [Fe/H] dispersion of 0.33 dex – ignoring error contribution – is substantially larger than that seen in any globular cluster, with the exception of the unusual system ω-Cen. In that cluster the total abundance range is about Δ[Fe/H] $\sim$ 1.4 dex: from −2 to −0.6 (e.g. Marino et al. 2011), and many subpopulations have been identified (e.g. Johnson & Pilachowski 2010).

Other clusters with established intrinsic [Fe/H] dispersions include M54 – a nuclear star cluster of the Sagittarius dSph – where $\sigma_{\rm int}([{\rm Fe/H}]) = 0.19$ (Carretta et al. 2010), and M22, where the interquartile range in [Fe/H] is $\sim$0.24 dex (Da Costa et al. 2009; Marino et al. 2009, 2011). There are a few clusters where the intrinsic dispersion is $\sim$0.10, namely NGC 1851 (Carretta et al. 2011), NGC 5824 (Da Costa, Held & Saviane 2014), and NGC 3201 (Simmerer et al. 2013). These globular clusters are outliers, and even amongst these unusual systems they largely do not match the abundance spread observed in the Aquarius stream (e.g. see fig. 4 in Simmerer et al. 2013). In fact, the Aquarius stream metallicity distribution – on its own – is large enough to be reconcilable with dSph galaxies like Fornax (e.g. Letarte et al. 2010). Similarly, the mean Aquarius stream metallicity and the log (L), $\langle$[Fe/H]$\rangle$ relation of Kirby et al. (2011) also suggest a relatively luminous system with $L_{\rm tot} \sim 10^{7.5}\,{\rm L}_{\odot}$ (Kirby et al. 2011). However, the Aquarius stream stars exhibit very different abundance ratios to Fornax. For example, [Ba/Y] (e.g. heavy/light s-process) abundance ratios in the Aquarius stream vary between −0.24 and +0.19, significantly lower than the [Ba/Y] $\geq$ 0.5 level generally observed in the present-day dSphs (Venn et al. 2004).

5.3 The Na–O relationship

Extensive studies of stars in globular clusters have revealed variations in light element abundances, most notably an anticorrelation in sodium and oxygen content (see Norris & Da Costa 1995; Carretta et al. 2009, and references therein). This chemical pattern has been identified in every well-studied globular cluster, although the

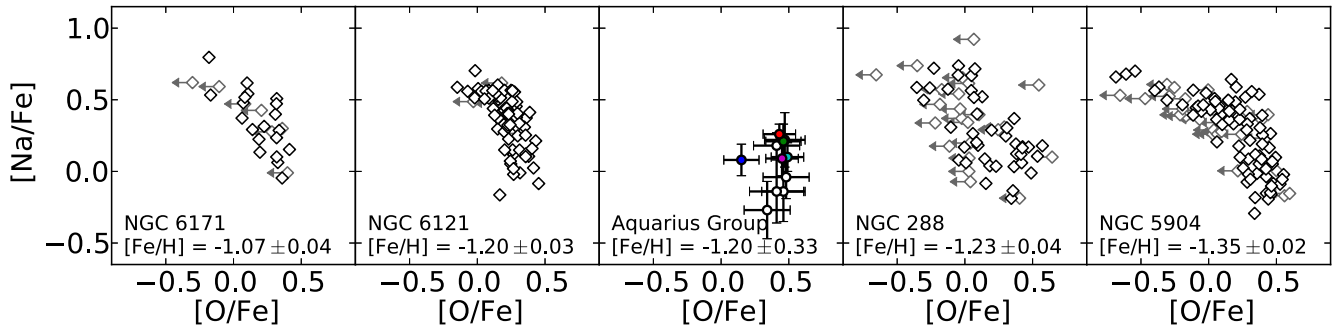

Figure 9. Oxygen and sodium abundances for four classical globular clusters with mean metallicities similar to the Aquarius stream (Carretta et al. 2009). All clusters demonstrate a Na–O anticorrelation. [O/Fe] and [Na/Fe] abundances from this study for the five Aquarius stream stars and standard stars (open circles) are shown in the middle panel. Colours for Aquarius stars is as per Fig. 3.

magnitude and shape of the anticorrelation varies from cluster to cluster. The direct connection between Na and O abundances requires an additional synthesis mechanism for Na, at least for the Na content that exceeds the Na in the primordial population.

Sodium is primarily produced through carbon burning in massive stars by the dominant ^{12}C(^{12}C, p)^{23}Na reaction. The final Na abundance is dependent on the neutron excess of the star, which slowly increases during carbon burning due to weak interactions (Arnett & Truran 1969). Massive stars ($>10\,M_{\odot}$) deliver their synthesized sodium to the interstellar medium through SN II explosions. Because the eventual SN II explosion is devoid of any significant β-decay processes, the neutron excess of the ejected material is representative of the pre-explosive abundance. The ejected material eventually condenses to form the next generation of stars, which will have a net increase in their neutron excess with respect to their predecessors. Thus an overall increase in the total sodium content *and* Na-production rate between stellar generations can be expected. The sodium content also becomes important for production of nickel during the SN II event (see Section 5.5) because ^{23}Na is the only stable isotope produced in significant quantities during C-burning.

Oxygen depletion is likely the result of complete CNO burning within the stellar interior. The nucleosynthetic pathways that produce the Na–O anticorrelation are well understood to be proton-capture nucleosynthesis at high temperatures (Prantzos, Charbonnel & Iliadis 2007). However, the temperatures required to produce these patterns are not expected within the interiors of globular cluster stars. While the exact mechanism for which these conditions occur remains under investigation, we can describe the abundance variation as an external oxygen depletion (or dilution) model with time. Through comparisons with existing globular clusters, we can make inferences on the star formation history of a system by measuring sodium and oxygen abundances in a sample of its stars.

Wylie-de Boer et al. (2012) measured sodium and oxygen abundances for four of their six Aquarius stream members. These abundance measurements exist for only three stars common to this study and Wylie-de Boer et al. (2012), as the data quality for J223811−104126 in the Wylie-de Boer et al. (2012) was too low to permit oxygen measurements. We have measured sodium and oxygen abundances for all of our stars, which are plotted in Figs 9 and 10.[5] These figures employ the corrected [O/Fe] value

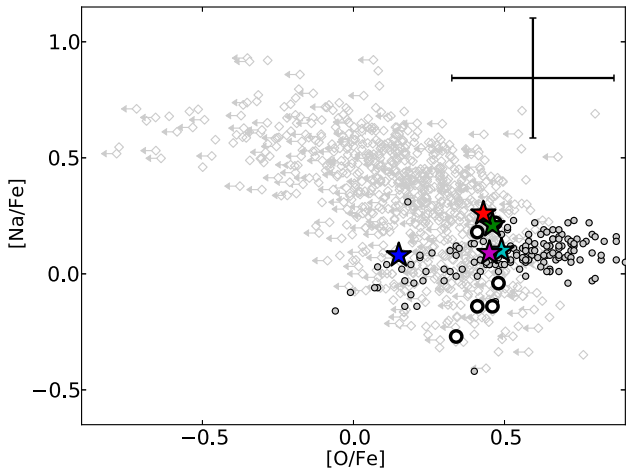

Figure 10. Oxygen and sodium abundances for disc/halo stars from Reddy et al. (2006) are shown as grey circles, and globular cluster stars from Carretta et al. (2009) are shown as diamonds. The Aquarius stream stars are also shown – following the same colours in Fig. 3 – illustrating how their [O/Fe], [Na/Fe] content is not dissimilar from Galactic stars. Although some standard stars (open circles) have lower [Na/Fe] abundances than the Reddy et al. (2006) sample, our values are consistent with Ishigaki et al. (2013), who did not measure O abundances.

for J223811−104126 rather than a conservative upper limit (see Section 4.3).

The Wylie-de Boer et al. (2012) measurements show two stars with solar levels of [Na/Fe] – identical to field star abundances for their metallicity – and two stars with slightly enhanced sodium content: J223504−152834 and J232619−080808. We also find J223504−152834 to be slightly sodium enhanced, whereas the second star in their study, J232619−080808, is not in our sample. We find the additional star not present in the Wylie-de Boer et al. (2012) sample, C2306265−085103, to be enhanced to almost the same level of J223504−152834 with [Na/Fe] = 0.26. The sodium-enhanced stars are not enhanced significantly above the total uncertainties, and they do not exhibit depletion of oxygen: their chemistry is not representative of a Na–O anticorrelation.

In the Aquarius sample we observe no intrinsic dispersion above the measurement uncertainty in [O/Fe] or [Na/Fe] (Fig. 10). A dispersion of 0.14 dex is observed for [O/Fe] (or 0.03 dex when J223811−104126 is excluded), which is only marginally larger than the mean total uncertainty of σ([O/Fe]) = 0.12 dex. Similarly for [Na/Fe], a dispersion of σ([Na/Fe]) = 0.08 dex is observed, when taking the uncertainties into account, is consistent with zero

[5] Although the Reddy et al. (2006) sample primarily consists of dwarfs/subgiants and we are observing primarily giants/subgiants, this does not affect our interpretation.

dispersion. We also see no significant variation in [C/Fe] outside the uncertainties, or relationship between [C/Fe] and [Na/Fe] (e.g. see Yong et al. 2008).

Now we consider the possibility that the Aquarius stars did originate in a globular cluster. Given the negligible dispersions present in [(O, Na, C)/Fe] (among other elements), the stars would be considered as members the primordial component, which comprises ∼33 per cent of the total population for any globular cluster (Carretta et al. 2009). The likelihood of randomly observing five globular cluster stars that all belong to the primordial component is 0.4 per cent. If the primordial component was a larger fraction (e.g. 40 or 50 per cent), this probability rises marginally, to 1 and 3 per cent, respectively. Given the dispersion in overall metallicity though, such a globular cluster would be an unusual object.

If the Aquarius stream is the result of a disrupted globular cluster, a large part of the picture must still be missing. Almost all of the Aquarius stream stars studied to date (either in this sample or the Wylie-de Boer et al. (2012) study), would be unambiguously classified as belonging to a 'primordial' component (see Carretta et al. 2009), with chemistry indistinguishable from field stars. In this scenario any inferred anticorrelation is equally explainable by observational uncertainties. Identifying more Aquarius stream members belonging to a postulated intermediate component with strong oxygen depletion, or perhaps members of an extreme component, would be convincing evidence for a Na–O anticorrelation and a globular cluster origin. Three stream stars identified to date (including two from this sample) might tenuously be classified as members of an intermediate population, with only a slight enhancement in sodium and no oxygen-depletion. Recall our [Na/Fe] abundance ratios appear systematically higher in our standard stars when compared to the literature sources listed in Table 3. Thus, if the strength of any Na–O relationship is to be used to vet potential disrupted hosts for the Aquarius stream, many more stream members will need to be identified and observed spectroscopically with high resolution and high S/N. In the absence of such data, no evidence exists for a Na–O anticorrelation in the Aquarius stream.

5.4 The Al–Mg relationship

Although not ubiquitous to every system, many globular clusters exhibit an anticorrelation between aluminium and magnesium. This is perhaps unsurprising, given the nucleosynthetic pathways for these elements. In addition to the CNO cycle operating during hydrogen burning, the Mg–Al chain can also operate under extreme temperatures ($T \sim 8 \times 10^6$ K; Arnould, Goriely & Jorissen 1999). Aluminium is produced by proton capture on to magnesium, beginning with ^{25}Mg to ^{26}Al. The relative lifetime of β-decay to proton capture allows for the production of unstable ^{27}Si through proton capture. Seconds later, the isotope decays to ^{27}Al, completing the ^{27}Si path of the Mg–Al chain. The alternative process from ^{26}Al involves β-decay to ^{26}Mg.

Wylie-de Boer et al. (2012) published magnesium and aluminium abundances for five stars in their Aquarius sample. No inverse correlation is present in their data; their abundances are indistinguishable from field stars. The [(Mg, Al)/Fe] abundance ratios tabulated in Table 8 are generally in agreement with the Wylie-de Boer et al. (2012) sample, and we also find no Mg–Al anticorrelation.

However it *is* surprising that we find such a strong positive relationship in [Mg/Fe] and [Al/Fe], with a best-fitting slope of [Al/Fe] = 2.08 × [Mg/Fe] − 0.57. If we exclude the chemically peculiar star C222531−145437, the slope decreases to [Al/Fe] = 0.96 × [Mg/Fe] − 0.16, a near 1:1 relationship. Even when a

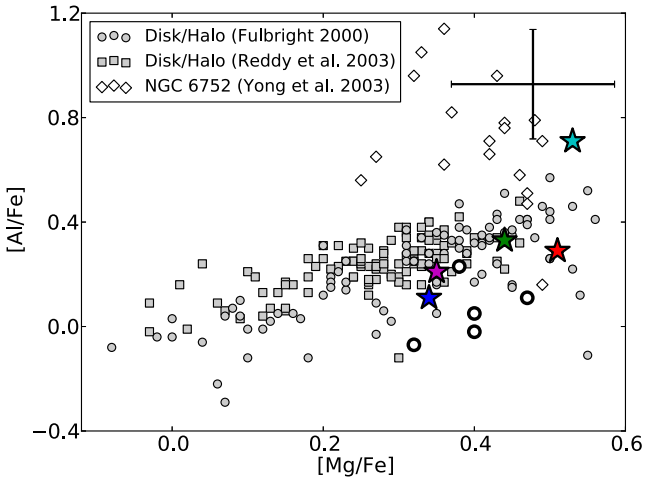

Figure 11. Magnesium and aluminium abundances for Aquarius stream stars, as well as Milky Way halo/disc stars from Reddy et al. (2003) and Fulbright (2000). Aquarius stars are coloured as described in Fig. 3.

Mg–Al anticorrelation is not detected in globular clusters, there is generally more scatter in [Al/Fe] at near-constant [Mg/Fe] (e.g. see Fig. 11 or Carretta et al. 2009). This is because Mg is much more abundant than Al, requiring only a small amount of Mg atoms to be synthesized to Al before the differences in Al abundance become appreciable, whilst the observed Mg abundance could remain within the uncertainties.

No classical globular clusters exhibit a positive correlation, and nor is such a pattern expected in globular clusters. However a positive relationship between magnesium and aluminium can result from SN II contributions to the local interstellar medium. Intermediate-mass ($\gtrsim$4 M$_\odot$) AGB models can also contribute towards a positive correlation between aluminium and magnesium. Under extreme temperatures ($T \gtrsim 300 \times 10^6$ K), substantial ^{25}Mg and ^{26}Mg are produced by α-capture on to ^{22}Ne by the ^{22}Ne(α,n)^{25}Mg and ^{22}Ne(α,γ)^{26}Mg reactions, respectively (e.g. Karakas et al. 2006). Depending on uncertain numerical details of stellar modelling, the third dredge-up can mix significant quantities of ^{25}Mg and ^{26}Mg into the photosphere, even more than the quantity of ^{26}Al produced through the Mg–Al cycle. Therefore, a positive relationship between magnesium and aluminium can occur if there has been significant contributions from intermediate-mass AGB stars, however this should also produce a Na–O anticorrelation (Karakas & Lattanzio 2003, but see results in Ventura, Carini & D'Antona 2011). The strong Mg–Al relationship observed provides additional chemical evidence against a globular cluster scenario for the Aquarius stream, and further suggests the chemistry is indicative of Milky Way disc stars.

5.5 The Na–Ni relationship

Detailed chemical studies of nearby disc stars have noted a correlation with [Na/Fe] and [Ni/Fe] abundance ratios (Fig. 12). This relationship was first hinted in Nissen & Schuster (1997), where the authors found eight stars that were underabundant in [α/Fe], [Na/Fe] and [Ni/Fe]. Interestingly, the authors noted that stars at larger Galactocentric radii were most deficient in these elements. Fulbright (2000) saw a similar signature: stars with low [Na/Fe] were only found at large (R_{GC} > 20 kpc) distances. Nissen & Schuster (1997) proposed that since the outer halo is thought to

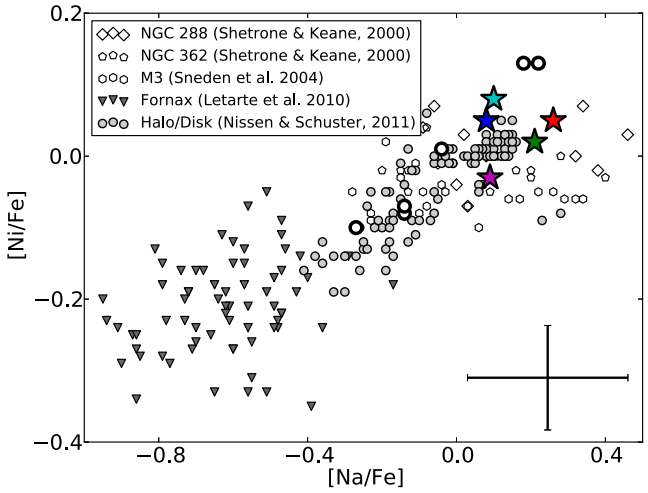

Figure 12. [Na/Fe] and [Ni/Fe] for Aquarius stream stars and for globular cluster, dSph, and field (halo/disc) stars. Aquarius targets are coloured as per Fig. 3. Stars from the most representative dSph galaxy, Fornax, are shown as downward triangles (▼). Fornax has been chosen as it lies closest to the luminosity that one would expect for an Aquarius host system, given its overall metallicity, metallicity dispersion, and the $\log(L)-\langle[\mathrm{Fe/H}]\rangle$ relationship (Kirby et al. 2011). The Nissen & Schuster (2011) plotted sample included halo stars, as well as low- and high-α disc members. As noted by Nissen & Schuster (1997, 2011), a positive Na–Ni relationship exists for field stars, with dSph members exhibiting strong depletion in both elements and globular cluster stars consistently showing an enhancement. Sodium and nickel content for Aquarius members indicate a dSph accretion origin is unlikely.

have been largely built up by accretion, the Na–Ni pattern may be a chemical indicator of merger history within the galaxy.

With additional data from Nissen & Schuster (2011), the Na–Ni relationship was found to be slightly steeper than originally proposed. The pattern exists only for stars with $-1.5 < [\mathrm{Fe/H}] < -0.5$, and is not seen in metal-poor dSph stars (Venn et al. 2004), providing a potentially useful indicator for investigating chemical evolution. However, it is crucial to note that although there are only a few dSph stars in the $-1.5 < [\mathrm{Fe/H}] < -0.5$ metallicity regime with [Na/Fe] and [Ni/Fe] measurements, they agree reasonably well with the Galactic trend.

The correlation between sodium and nickel content is the nucleosynthetic result of neutron capture in massive stars. As previously discussed, the total Na abundance is controlled by the neutron excess, which limits the production of ^{58}Ni during SN II events. When the inevitable SN begins, the core photodissociates into neutrons and protons, allowing the temporary creation of ^{56}Ni before it decays to ^{56}Fe. A limited amount of ^{54}Fe is also formed, which is the main source of production for the stable ^{58}Ni isotope through α-capture. The quantity of ^{54}Fe (and hence ^{58}Ni) produced is dependent on the abundance of neutron-rich elements during the explosion. As ^{23}Na is a relatively plentiful neutron source with respect to other potential sources (like ^{13}C), the post-SN ^{58}Ni abundance is driven by the pre-explosion ^{23}Na content. Thus, through populations of massive stars undergoing C-burning, a positive correlation between sodium and nickel can be expected.

Stars originating in dSph galaxies and globular clusters have very different chemical enrichment environments. Consequently, both types of systems exhibit chemistry that reflects their nucleosynthetic antiquity. Stars in dSphs do not demonstrate enhanced sodium or nickel content with respect to iron, as there has been a relatively small lineage of massive stars undergoing SN. In contrast, globular cluster stars do have elevated [Na/Fe] and [Ni/Fe] signatures. This sharp contrast between dSph and globular cluster star chemistry is highlighted in Fig. 12. Given the extended star formation within the Milky Way disc, globular cluster stars and disc stars are indiscernible in the Na/Ni plane: they both show an extended contribution of massive stars. The most that can be inferred from the Na and Ni abundances of Aquarius stream stars is that their enrichment environment is less like a dSph galaxy, and more representative of either a globular cluster, or the Milky Way disc.

5.6 The chemically peculiar star C222531−145437

In almost every element with respect to iron, C222531−145437 is distinct from the other Aquarius stream stars. It is overabundant in light and neutron-capture elements, with a high barium abundance of $[\mathrm{Ba/Fe}] = 0.68$. This value is well in excess of the halo ($[\mathrm{Ba/Fe}] \sim 0.0$) – and our other Aquarius stream stars – which vary between -0.02 to 0.15 dex.

Here we discuss the possibility that an unseen companion has contributed to the surface abundances of C222531−145437. Although no radial velocity variations were observed between exposures, we do not have a sufficient baseline to detect such variation. The abundances of heavy elements produced by AGB stars have a high dependence on the initial metallicity and mass. Low-mass ($\lesssim 3\,\mathrm{M}_\odot$) AGB stars of low metallicity produce high fractions of heavy *s*-process elements compared to their light *s*-process counterparts (Busso et al. 2001). As such, [Ba/Y] is a useful indicator for considering contributions from a low-mass AGB companion. For C222531−145437, $[\mathrm{Ba/Y}] = -0.17$, which is much lower than expected if a low-mass AGB star was responsible for the heavy element enhancements ($[\mathrm{Ba/Y}] \sim 0.5$ as shown in Fig. 13; see also Cristallo et al. 2009). If mass transfer from an AGB companion has occurred very recently, non-negligible amounts of technetium, produced by the AGB star, remain visible in the companion's photosphere before ^{99}Tc decays over ∼2 myr (Brown et al. 1990; Van Eck & Jorissen 1999; Uttenthaler et al. 2011). We saw no technetium absorption at λλ4049, 4238 or 4297 in the spectrum of C222531−145437. Intermediate-mass (3–5 $\mathrm{M}_\odot$) AGB stars also cannot explain the abundances for C222531−145437: using recently computed intermediate-mass AGB *s*-process yields for 3–5 $\mathrm{M}_\odot$ for a star of $[\mathrm{Fe/H}] \approx -1.2$ (Fishlock & Karakas in preparation) the resulting surface abundances do not match the observations (Fig. 13). Therefore, we find no reason to suspect the heavy

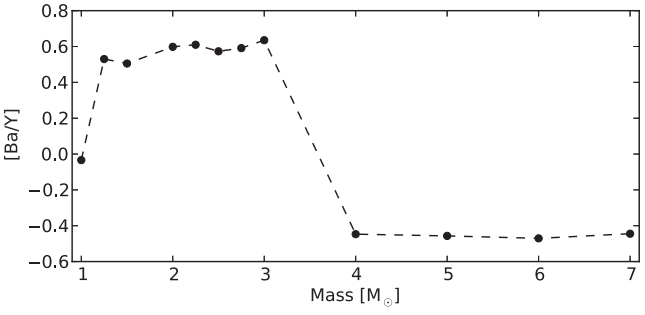

Figure 13. Distribution of the final surface abundance of [Ba/Y] with initial mass for each of the AGB models calculated for $Z = 0.001$ (Fishlock et al., in preparation). The ratio of [Ba/Y] can be used as an indicator of the initial mass of the AGB companion where the low-mass AGB models show a higher [Ba/Y] ratio compared to the intermediate-mass AGB models.

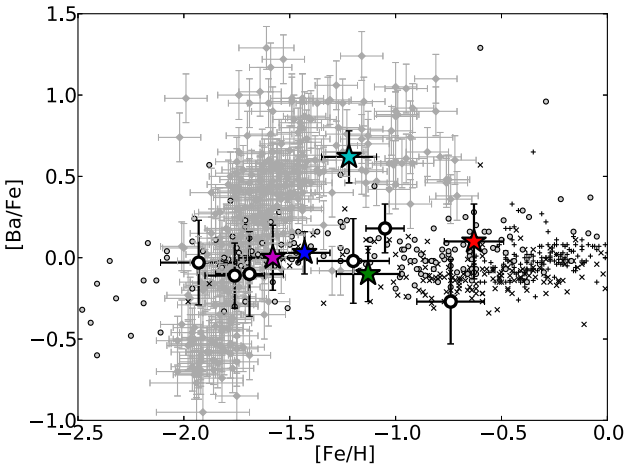

Figure 14. [Fe/H] and [Ba/Fe] for halo/disc stars (black) from Fulbright (2000), Reddy et al. (2003), Reddy et al. (2006) and ω-Cen RGB stars (grey) from Francois, Spite & Spite (1988), Smith et al. (2000) and Marino et al. (2011). Similar trends are observed for other heavy elements in ω-Cen members. Aquarius stars are coloured as per Fig. 3.

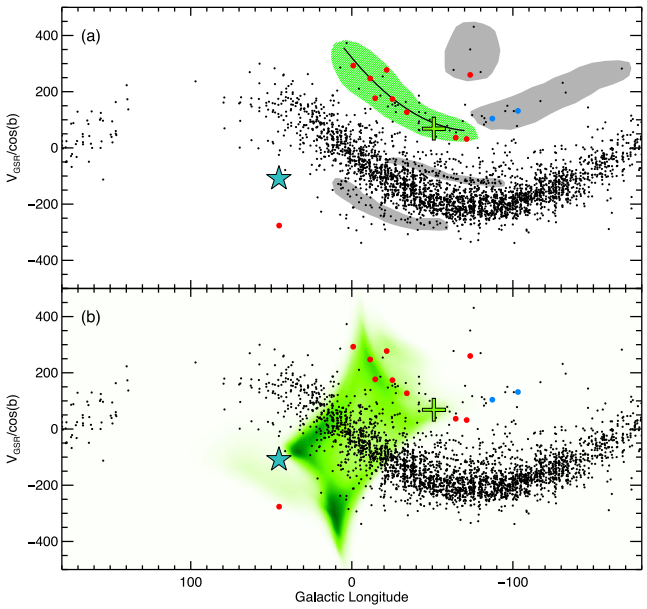

Figure 15. Panel (a) shows the distribution of giant stars in the GGSS (Majewski et al. 2012) in Galactic longitude and $V_{GSR}/\cos(b)$ after excluding stars with $|b| > 60°$. Stars from the GGSS sample believed to be ω-Cen tidal debris are shown in green shading. Red points are stars from the GGSS sample with abundances that follow the ω-Cen [Ba/Fe]–[Fe/H] pattern. Blue points are those with high-resolution spectra that do not follow this trend. Grey shading highlights other potential halo substructures from their study. Panel (b) shows the probability distribution of ω-Cen tidal debris from 4050 simulations. The ω-Cen core is shown as a green cross and the cyan star represents C222531−145437, falling almost precisely where a relatively high probability of ω-Cen tidal debris is expected.

element enhancement in C222531−145437 is the result of mass transfer from an AGB companion.

Stars in ω-Cen show large overabundances of *s*-process elements compared to the Galaxy (Norris & Da Costa 1995; Johnson & Pilachowski 2010; Stanford, Da Costa & Norris 2010). M22 also hosts an *s*-process rich population (Marino et al. 2011). Like the Aquarius comoving group, both clusters are relatively close to the Sun: 5.2 kpc and 3.2 kpc, respectively. M22 has a mean metallicity of [Fe/H] ~ -1.7 and a range between $-2.0 <$ [Fe/H] < -1.6 dex, making an association between C222531−145437 and M22 unlikely. Similarly, C222531−145437 is unlikely to be associated with the metal-rich Argus association (IC 2391; De Silva et al. 2013), which also shows large enhancement in *s*-process abundances. Other groups have identified field stars enriched in *s*-process elements, which have generally been associated as tidal debris from ω-Cen (Wylie-de Boer et al. 2010; Majewski et al. 2012). The high *s*-process abundance ratios and overall metallicity of C222531−145437 ([Fe/H] = −1.22) suggests this star may also be a remnant from the tidal disruption process. This is illustrated in Fig. 14. In contrast to the comparison field stars, C222531−145437 also demonstrates a high [Eu/Fe] abundance ratio of +0.42, which is also consistent with studies of ω-Cen stars (e.g. see fig. 10 of Johnson & Pilachowski 2010).

ω-Cen has a retrograde orbit with low inclination. Many groups simulating this orbit have predicted retrograde tidal debris to occur near the solar circle (Dinescu 2002; Bekki & Freeman 2003; Tsuchiya, Dinescu & Korchagin 2003; Tsuchiya, Korchagin & Dinescu 2004). Subsequent searches for ω-Cen debris in the solar neighbourhood have led to tantalizing signatures of debris. From over 4 000 stars targeted by Da Costa & Coleman (2008) in the vicinity of the cluster's tidal radius, only six candidate debris members were recovered, consistent with tidal stripping occurring long ago. Using data from the Grid Giant Star Survey (GGSS), an all-sky search looking for metal-poor giant stars, Majewski et al. (2012) identified 12 stream candidates. In addition, Majewski et al. (2012) performed 4050 simulations in order to predict likely locations for ω-Cen tidal debris. The results of their simulation are replicated in Fig. 15, where the location of C222531−145437 is also shown. The velocity and position of C222531−145437 align almost precisely where Majewski et al. (2012) predict a high probability of tidal debris. More interestingly, the angular momentum and orbital energy for C222531−145437 (Fig. 4) matches excellently for ω-Cen cluster stars as well as its previously identified tidal remnants (Wylie-de Boer et al. 2010). The chemical and phase-space information strongly suggests that C222531−145437 is associated with the remnants of tidal stripping that occurred as the proto-ω-Cen fell into the Galaxy (Bekki & Freeman 2003).

In the Aquarius stream discovery paper, Williams et al. (2011) attempted to exclude possible known progenitors for the Aquarius stream. On the basis of metallicity, distance, proper motions, transverse velocities and orbital energies, the authors were able to exclude all known Milky Way satellites with the notable exception of ω-Cen. Although the Aquarius stream metallicity distribution is not dissimilar from a known subpopulation in ω-Cen, the individual chemical abundances are quite distinct. The strong *s*-process enhancement with overall metallicity is not observed in the rest of our sample. Thus, with the exception of C222531−145437, the Aquarius members do not have a chemistry that is synonymous with ω-Cen tidal debris. It will be most interesting to learn how many other members of the Aquarius stream are tidal remnants of ω-Cen, given the frequency of these objects is quite low (e.g. see Da Costa & Coleman 2008; Majewski et al. 2012).

5.7 Disrupted disc/halo stars – signature of a disc–satellite interaction?

Since the Aquarius stream is kinematically coherent, it has been assumed that the moving group has been accreted on to the Milky

Way from a tidally disrupted satellite. The chemical abundances presented in this study do not favour an accretion scenario from a globular cluster or a dSph; there is conflicting evidence for either hypothesis. As it stands, the moving group appears chemically indistinguishable from thick disc/halo stars. These results force us to consider other scenarios that may replicate the observations.

The Aquarius stream has an unusually wide intrinsic velocity distribution. Generally a stellar stream is considered kinematically 'cold' when its velocity dispersion is $\lesssim 8\,\mathrm{km\,s^{-1}}$. We find the velocity dispersion from five members to be $\sim 30\,\mathrm{km\,s^{-1}}$, consistent with Williams et al. (2011). Hypotheses invoked to explain the Aquarius moving group must account for the high velocity dispersion.

There are other moving groups in the Milky Way that were initially considered as tidal tails from disrupted satellites but are no longer regarded as accretion events. We now list some examples. The Hercules moving group is significantly offset from the bulk of the velocity distribution observed in the field. Members of the Hercules group exhibit a wide range of metallicities and ages (Bensby et al. 2007; Bovy & Hogg 2010). Furthermore, Hercules group stars have [X/Fe] abundance ratios at a given [Fe/H] that are *not* substantially different from the thin or thick disc. The Hercules group kinematics are well replicated in simulations by stars in the outer disc resonating with the bar in the central region of the Milky Way (Dehnen 2000; Fux 2001), and strong predictions are made for disc velocity distributions that would lend further weight to this hypothesis (Bovy 2010). Similarly, the Canis Major stellar overdensity was also first considered to be an accretion feature from the postulated Canis Majoris dSph galaxy (Martin et al. 2004). However, Momany et al. (2004) demonstrate that the star counts, proper motions, photometry and kinematics of the 'accreted feature' can be easily explained by the warp and flare in the outer thick disc. The Monoceros ring (Newberg et al. 2002; Jurić et al. 2008) is perhaps another example of such an occurrence, as similar features naturally emerge as a consequence of galaxy–satellite interactions (Purcell et al. 2011), which has prompted considerable discussion (Lopez-Corredoira et al. 2012). It is clear that not all kinematic groups are attributable to accretion events; in many scenarios a Galactic origin is more likely, and simpler.

We hypothesize that the Aquarius group is the result of displaced stars from a perturbation in the thick disc. That is, the stars are Galactic in origin but have been displaced by a disc–satellite interaction. Minor mergers can significantly disrupt the host galaxy (Villalobos & Helmi 2008), producing extended spatial and kinematic structure in the process. Minchev et al. (2009) proposed that such a perturbation would cause a Galactic 'ringing' effect in the neighbourhood surrounding the merger site, analogous to the resulting compression wave propagating outwards from a stone falling in water. Stars move closer together in the wave peak, a signature which is observable in the velocities and orbital motions of nearby stars. This signature is most prominent in the U–V velocity plane as concentric circles (Gómez et al. 2012a), and dissolves over time (a few Gyr, depending on the mass of the perturber). After the U–V velocity signature dissipates, a clear signature in angular momentum and orbital energy (L_Z, E) persists for long periods following the merger (e.g. see Gómez et al. 2012a).

Through Milky Way–Sagittarius simulations, Purcell et al. (2011) found that these disc–satellite interactions can explain ringing perturbations within the disc. Additionally, Widrow et al. (2012) and Gómez et al. (2012b) independently observed these phenomena – a *'wavelike perturbation'*, as Widrow described – in the SDSS and SEGUE catalogues. More recently, Gómez et al. (2013) proposed that these patterns were induced by the Sagittarius dSph interacting with the disc. Their simulations reproduce the observed north–south asymmetries and vertical wave-like structure, and show that the amplitude of these oscillations is strongly dependent on Galactocentric distance. Combined with the oscillating vertical motions with the $U-V$ velocity pattern, corrugated waves are observed as a result of the interaction.

The stars in these oscillations should exhibit a wide range of ages, metallicities and a large spread in velocity dispersion. Thus, resultant oscillations following a disc–satellite interaction can satisfactorily explain the existence of the Aquarius moving group. We do not observe a distinct coherence in the $U-V$ velocity plane in our data, but the angular momentum and orbital energies for Aquarius members qualitatively reproduces the theoretically predicted pattern by Gómez et al. (2012a) in a retrograde direction. The extent and gradient of this L_Z–E signature is dependent on the mass of the perturber and the time since infall. Although our sample size is minute – and the sample size would still be small even if all Aquarius members had reliable orbits – the fact that we see no $U-V$ velocity coherence (Fig. 3) is consistent with the observed L_Z–E pattern: signatures in the L_Z–E plane (Fig. 4) become more extended over time as the U–V signature dissipates. This is consistent with a disc–satellite interaction occurring in the disc approximately a few Gyr ago.

The Aquarius moving group resides at an intermediate latitude ($b \approx -55^\circ$) and with a radial distance of up to $\sim 5\,\mathrm{kpc}$ for some stars, the stars are slightly out of the plane. This is not inconsistent with a disc–satellite interaction, as similar features in the Galactic field star population naturally emerge. Gómez et al. (2013) find that a significant fraction of the total energy goes into vertical perturbations. While the mean vertical distance $\langle Z \rangle$ in their simulations is near zero, this is an average of disc particles at all plane heights – positive and negative – and the dispersions around $\langle Z \rangle$ are very large (Gómez, private communication). Moreover, Gómez et al. (2013) were only able to reliably track particles up to $|Z| \approx 1.4\,\mathrm{kpc}$ due to a finite number of particles in each cell volume.

If the Aquarius group is a feature of a disc-satellite interaction, the perturber must have a mass of the order of a large globular cluster or a dSph satellite to produce the residual pattern in orbital energy and angular momenta. The Sagittarius dSph galaxy is an obvious candidate, but ω-Cen is also a possible perturber. On the basis on position, velocities, chemical abundances and orbit, we identify C222531−145437 was highly likely stripped from ω-Cen in the past. Thus, it is plausible that ω-Cen has disrupted Galactic stars as it passed through the plane, adding to any other oscillating modes rippling through the disc, resulting in what we now observe as the Aquarius stream.

6 CONCLUSIONS

We have presented a detailed chemical and dynamical analysis for 5 members of the recently discovered Aquarius stream from data taken with the MIKE spectrograph on the Magellan Clay telescope. Hereafter, we solely refer to the discovery as a moving group instead of a stellar stream, as we find no evidence that the group is a tidal tail of a disrupted satellite. The main conclusions are as follows.

(i) The Aquarius stream is not monometallic. A wide spread in metallicities is observed, with [Fe/H] ranging from −0.63 to −1.58 in just five members. The mean of the sample is [Fe/H] = −1.20 and the dispersion is $\sigma([\mathrm{Fe/H}]) = 0.33$ dex.

(ii) No Na–O anticorrelation is observed in the Aquarius group. Two members have slightly enhanced levels of sodium with respect

to iron. If the candidates were *known globular cluster members*, they would be classified as belonging to either the primordial component, or at most, tenuous membership could be argued for the lower envelope of the intermediate group.

(iii) We find no evidence that the Aquarius group is the result of a disrupted classical globular cluster. The large [Fe/H] variation severely limits the number of possible parent hosts, and both the extreme and intermediate component of the Na–O anticorrelation have not been observed. A strong positive Mg–Al relationship is observed, reminiscent of Milky Way field stars. In total, high-resolution spectra exists for more than half of the stream.

(iv) The moving group shows an α-enhancement of $[\alpha/\mathrm{Fe}] = +0.40$ dex, similar to the Milky Way, and distinct to that typically observed in stars in dSph galaxies with comparable metallicities.

(v) Aquarius members are enhanced in [Na/Fe] and [Ni/Fe] to levels typically observed in either the thick disc or globular clusters. These levels of [Na/Fe] and [Ni/Fe] enhancement are not observed in stars from dSph galaxies. Low [Ba/Y] abundance ratios are also observed in the Aquarius group, in conflict with chemistry of present-day dSph galaxies. Thus, on the basis of [(Na, Ni, α)/Fe] and [Ba/Y] abundance ratios, it is unlikely the Aquarius moving group is the result of a tidally disrupted dSph galaxy.

(vi) One of the candidates, C222531−145437, has an abundance pattern that is clearly distinct from the other Aquarius members, most notably in barium where [Ba/Fe] = 0.68. We exclude the possibility that the abundance variations have resulted from an AGB companion.

(vii) The position and velocity of C222531−145437 agrees excellently where simulations by Majewski et al. (2012) predict large amounts of ω-Cen tidal debris, and the orbital energy and angular momenta are consistent with the ω-Cen cluster. The chemical and phase-space information suggests that C222531−145437 is a rare tidal debris remnant from the globular cluster ω-Cen. Removing C222531−145437 from the Aquarius sample does not extinguish or diminish any of the aforementioned conclusions.

(viii) While no evidence exists for an accreted origin, and the Aquarius group members are indistinguishable from thick disc/halo stars, we hypothesize the moving group is the result from a disc–satellite interaction. We see no coherent pattern in the *U*–*V* plane from Monte Carlo simulations, but the orbital energies and angular momenta for the Aquarius group qualitatively reproduces patterns predicted by Gómez et al. (2012a). This is consistent with a minor merger in the Milky Way thick disc occurring perhaps up to a few Gyr ago. Given the location and velocity of the Aquarius group, and the identification of C222531−145437 as a star tidally stripped from ω-Cen, it is plausible that the Milky Way–ωCen interaction sufficiently perturbed outer disc/halo stars to produce what we now observe as the Aquarius group.

It is clear that not all moving groups are tidal tails of disrupted satellites, and that the structure of the Milky Way is indeed complex. While we find no chemical evidence that the Aquarius group is a tidal tail from a disrupted satellite, we propose the members are Galactic in origin, and the group is a result of a disc–satellite interaction. Thus, although the Aquarius group has not been accreted on to the Galaxy, it certainly adds to the rich level of kinematic substructure within the Milky Way.

ACKNOWLEDGEMENTS

We thank the anonymous referee for constructive comments which improved this paper. We are indebted to David Nidever and Steven Majewski for kindly replicating a plot from their ω-Cen simulations (Fig. 15 in this paper) which helped to place C222531−145437 in context of the cluster's tidal debris. ARC acknowledges the financial support through the Australian Research Council Laureate Fellowship LF0992131, and from the Australian Prime Minister's Endeavour Award Research Fellowship, which facilitated his research at MIT. SK and GDC acknowledge research support from the Australian Research Council through Discovery Project grant DP120101237, while AA-B acknowledges research support from the same source through Super Science Fellowship program FS110200016, and through FONDECYT Chile (3100013). AF acknowledges support from NSF grant AST-1255160. Australian access to the Magellan Telescopes was supported through the National Collaborative Research Infrastructure Strategy of the Australian Federal Government. This publication makes use of data products from the Two Micron All Sky Survey, which is a joint project of the University of Massachusetts and the Infrared Processing and Analysis Center/California Institute of Technology, funded by the National Aeronautics and Space Administration and the National Science Foundation.

REFERENCES

Allende Prieto C., Lambert D. L., Asplund M., 2001, ApJ, 556, L63
Alonso A., Arribas S., Martínez-Roger C., 1999, A&AS, 140, 261
Aoki W. et al., 2007, ApJ, 660, 747
Arnett W. D., Truran J. W., 1969, ApJ, 157, 339
Arnould M., Goriely S., Jorissen A., 1999, A&A, 347, 572
Asplund M., García Pérez A. E., 2001, A&A, 372, 601
Asplund M., Grevesse N., Sauval A. J., Scott P., 2009, ARA&A, 47, 481
Barber C., Dobkin D., Huhdanpaa H., 1996, ACM Trans. Math. Softw., 22, 469
Baumueller D., Gehren T., 1997, A&A, 325, 1088
Bekki K., Freeman K. C., 2003, MNRAS, 346, L11
Bell E. F. et al., 2008, ApJ, 680, 295
Belokurov V. et al., 2007, ApJ, 658, 337
Bensby T., Oey M. S., Feltzing S., Gustafsson B., 2007, ApJ, 655, L89
Bergemann M., Pickering J. C., Gehren T., 2010, MNRAS, 401, 1334
Bernstein R., Shectman S. A., Gunnels S. M., Mochnacki S., Athey A. E., 2003, Proc. SPIE, 4841, 1694
Biémont E., Palmeri P., Quinet P., 1999, Ap&SS, 269, 635
Bovy J., 2010, ApJ, 725, 1676
Bovy J., Hogg D. W., 2010, ApJ, 717, 617
Breddels M. A. et al., 2010, A&A, 511, 90
Brown J. A., Smith V. V., Lambert D. L., Dutchover Jr, E., Hinkle K. H., Johnson H. R., 1990, AJ, 99, 1930
Bullock J. S., Johnston K. V., 2005, ApJ, 635, 931
Burnett B., Binney J., 2010, MNRAS, 407, 339
Burris D. L., Pilachowski C. A., Armandroff T. E., Sneden C., Cowan J. J., Roe H., 2000, ApJ, 544, 302
Busso M., Gallino R., Lambert D. L., Travaglio C., Smith V. V., 2001, ApJ, 557, 802
Carretta E. et al., 2009, A&A, 505, 117
Carretta E. et al., 2010, A&A, 520, A95
Carretta E., Lucatello S., Gratton R. G., Bragaglia A., D'Orazi V., 2011, A&A, 533, A69
Casagrande L., Ramírez I., Meléndez J., Bessell M., Asplund M., 2010, A&A, 512, 54
Casey A. R., 2014, preprint (arXiv:1405.5968)
Castelli F., Kurucz R. L., 2003, in Piskunov N., Weiss W. W., Gray D. F., eds, IAU Symp. 210, Modelling of Stellar Atmospheres. Astron. Soc. Pac., San Francisco, p. 20
Cayrel R. et al., 2004, A&A, 416, 1117
Cristallo S., Straniero O., Gallino R., Piersanti L., Domínguez I., Lederer M. T., 2009, ApJ, 696, 797

Da Costa G. S., Coleman M. G., 2008, AJ, 136, 506
Da Costa G. S., Held E. V., Saviane I., Gullieuszik M., 2009, ApJ, 705, 1481
Da Costa G. S., Held E. V., Saviane I., 2014, MNRAS, 438, 3507
De Silva G. M., D'Orazi V., Melo C., Torres C. A. O., Gieles M., Quast G. R., Sterzik M., 2013, MNRAS, 431, 1005
Dehnen W., 2000, AJ, 119, 800
Dinescu D. I., 2002, in van Leeuwen F., Hughes J. D., Piotto G., eds, ASP Conf. Ser. Vol. 265, Omega Centauri, A Unique Window into Astrophysics. Astron. Soc. Pac., San Francisco, p. 365
Dotter A., Chaboyer B., Jevremović D., Kostov V., Baron E., Ferguson J. W., 2008, ApJS, 178, 89
Drake A. J. et al., 2013, ApJ, 765, 154
Francois P., Spite M., Spite F., 1988, A&A, 191, 267
Frebel A., Casey A. R., Jacobson H. R., Yu Q., 2013, ApJ, 769, 57
Freeman K., Bland-Hawthorn J., 2002, ARA&A, 40, 487
Frischknecht U., Hirschi R., Thielemann F.-K., 2012, A&A, 538, 2
Fulbright J. P., 2000, AJ, 120, 1841
Fux R., 2001, A&A, 373, 511
García Pérez A. E., Asplund M., Primas F., Nissen P. E., Gustafsson B., 2006, A&A, 451, 621
Gómez F. A., Minchev I., Villalobos, Á., O'Shea B. W., Williams M. E. K., 2012a, MNRAS, 419, 2163
Gómez F. A. *et al.*, 2012b, MNRAS, 423, 3727
Gómez F. A., Minchev I., O'Shea B. W., Beers T. C., Bullock J. S., Purcell C. W., 2013, MNRAS, 429, 159
Gratton R. G., Sneden C., 1991, A&A, 241, 501
Gratton R. G., Sneden C., Carretta E., Bragaglia A., 2000, A&A, 354, 169
Grevesse N., Sauval A. J., 1998, Space Sci. Rev., 85, 161
Helmi A., 2008, A&A Rev., 15, 145
Helmi A., White S. D. M., 1999, MNRAS, 307, 495
Henden A. A., Levine S. E., Terrell D., Smith T. C., Welch D., 2012, J. Am. Assoc. Var. Star Obser., 40, 430
Ishigaki M. N., Aoki W., Chiba M., 2013, ApJ, 771, 67
Johnson J. A., 2002, ApJS, 139, 219
Johnson C. I., Pilachowski C. A., 2010, ApJ, 722, 1373
Jurić M. et al., 2008, ApJ, 673, 864
Karakas A. I., Lattanzio J. C., 2003, Publ. Astron. Soc. Aust., 20, 279
Karakas A. I., Lugaro M. A., Wiescher M., Görres J., Ugalde C., 2006, ApJ, 643, 471
Kirby E. N., Lanfranchi G. A., Simon J. D., Cohen J. G., Guhathakurta P., 2011, ApJ, 727, 78
Kobayashi C., Nakasato N., 2011, ApJ, 729, 16
Kobayashi C., Karakas A. I., Umeda H., 2011, MNRAS, 414, 3231
Kurucz R., Bell B., eds, 1995, Kurucz CD-ROM No. 23. Smithsonian Astrophysical Observatory, Cambridge, MA, p. 23
Lawler J. E., Bonvallet G., Sneden C., 2001a, ApJ, 556, 452
Lawler J. E., Wickliffe M. E., den Hartog E. A., Sneden C., 2001b, ApJ, 563, 1075
Letarte B. et al., 2010, A&A, 523, A17
Lopez-Corredoira M., Moitinho A., Zaggia S., Momany Y., Carraro G., Hammersley P. L., Cabrera-Lavers A., Vazquez R. A. et al., 2012, (arXiv:1207.2749)
Majewski S. R., Nidever D. L., Smith V. V., Damke G. J., Kunkel W. E., Patterson R. J., Bizyaev D., García Pérez A. E., 2012, ApJ, 747, L37
Marino A. F., Milone A. P., Piotto G., Villanova S., Bedin L. R., Bellini A., Renzini A., 2009, A&A, 505, 1099
Marino A. F. et al., 2011, A&A, 532, 8
Martin N. F., Ibata R. A., Bellazzini M., Irwin M. J., Lewis G. F., Dehnen W., 2004, MNRAS, 348, 12
Meyer B. S., 1994, ARA&A, 32, 153
Minchev I., Quillen A. C., Williams M., Freeman K. C., Nordhaus J., Siebert A., Bienaymé O., 2009, MNRAS, 396, L56
Miyamoto M., Nagai R., 1975, PASJ, 27, 533
Momany Y., Zaggia S. R., Bonifacio P., Piotto G., De Angeli F., Bedin L. R., Carraro G., 2004, A&A, 421, L29
Munari U., Sordo R., Castelli F., Zwitter T., 2005, A&A, 442, 1127
Navarro J. F., Frenk C. S., White S. D. M., 1997, ApJ, 490, 493
Newberg H. J. et al., 2002, ApJ, 569, 245
Nissen P. E., Schuster W. J., 1997, A&A, 326, 751
Nissen P. E., Schuster W. J., 2010, A&A, 511, L10
Nissen P. E., Schuster W. J., 2011, A&A, 530, 15
Nissen P. E., Chen Y. Q., Schuster W. J., Zhao G., 2000, A&A, 353, 722
Nordström B. et al., 2004, A&A, 418, 989
Norris J. E., Da Costa G. S., 1995, ApJ, 441, L81
Norris J. E., Ryan S. G., Beers T. C., 1996, ApJS, 107, 391
Norris J. E., Ryan S. G., Beers T. C., 2001, ApJ, 561, 1034
Plez B., Masseron T., Van Eck S., 2008, in ASP Conf. Ser., Vol. 384, Cool Stars, Stellar Systems and the Sun. Astron. Soc. Pac., San Francisco
Prantzos N., Charbonnel C., Iliadis C., 2007, A&A, 470, 179
Purcell C. W., Bullock J. S., Tollerud E. J., Rocha M., Chakrabarti S., 2011, Nature, 477, 301
Ramírez I., Meléndez J., 2005, ApJ, 626, 465
Reddy B. E., Tomkin J., Lambert D. L., Allende Prieto C., 2003, MNRAS, 340, 304
Reddy B. E., Lambert D. L., Allende Prieto C., 2006, MNRAS, 367, 1329
Robin A. C., Reylé C., Derrière S., Picaud S., 2003, A&A, 409, 523
Roederer I. U., Sneden C., Thompson I. B., Preston G. W., Shectman S. A., 2010, ApJ, 711, 573
Schlegel D. J., Finkbeiner D. P., Davis M., 1998, ApJ, 500, 525
Schönrich R., 2012, MNRAS, 427, 274
Searle L., Zinn R., 1978, ApJ, 225, 357
Sharma S., Bland-Hawthorn J., Johnston K. V., Binney J., 2011, ApJ, 730, 3
Shetrone M. D., 1996, AJ, 112, 1517
Siebert A. et al., 2011, AJ, 141, 187
Simmerer J., Ivans I. I., Filler D., Francois P., Charbonnel C., Monier R., James G., 2013, ApJ, 764, L7
Skrutskie M. F. et al., 2006, AJ, 131, 1163
Smith V. V., Suntzeff N. B., Cunha K., Gallino R., Busso M., Lambert D. L., Straniero O., 2000, AJ, 119, 1239
Sneden C. A., 1973, PhD thesis, The University of Texas at Austin
Sobeck J. S. et al., 2011, AJ, 141, 175
Stanford L. M., Da Costa G. S., Norris J. E., 2010, ApJ, 714, 1001
Steinmetz M. et al., 2006, AJ, 132, 1645
Travaglio C., Gallino R., Arnone E., Cowan J., Jordan F., Sneden C., 2004, ApJ, 601, 864
Tsuchiya T., Dinescu D. I., Korchagin V. I., 2003, ApJ, 589, L29
Tsuchiya T., Korchagin V. I., Dinescu D. I., 2004, MNRAS, 350, 1141
Uttenthaler S. et al., 2011, A&A, 531, A88
Van Eck S., Jorissen A., 1999, A&A, 345, 127
Venn K. A., Irwin M., Shetrone M. D., Tout C. A., Hill V., Tolstoy E., 2004, AJ, 128, 1177
Ventura P., Carini R., D'Antona F., 2011, MNRAS, 415, 3865
Villalobos Á., Helmi A., 2008, MNRAS, 391, 1806
Widrow L. M., Gardner S., Yanny B., Dodelson S., Chen H.-Y., 2012, ApJ, 750, L41
Williams M. E. K. et al., 2011, ApJ, 728, 102
Wylie-de Boer E., Freeman K., Williams M., 2010, AJ, 139, 636
Wylie-de Boer E., Freeman K., Williams M., Steinmetz M., Munari U., Keller S., 2012, ApJ, 755, 35
Yong D., Carney B. W., Teixera de Almeida M. L., 2005, AJ, 130, 597
Yong D., Meléndez J., Cunha K., Karakas A. I., Norris J. E., Smith V. V., 2008, ApJ, 689, 1020
Zwitter T. et al., 2008, AJ, 136, 421
Zwitter T. et al., 2010, A&A, 522, A54

SUPPORTING INFORMATION

Additional Supporting Information may be found in the online version of this article:

Table 2. List of atomic transitions and equivalent width measurements for programme and standard stars.
Table 9. Abundance uncertainties due to errors in stellar parameters (http://mnras.oxfordjournals.org/lookup/suppl/doi:10.1093/mnras/stu1031/-/DC1).

Please note: Oxford University Press are not responsible for the content or functionality of any supporting materials supplied by the authors. Any queries (other than missing material) should be directed to the corresponding author for the article.

This paper has been typeset from a TEX/LATEX file prepared by the author.